An efficient mass-preserving interface-correction level set/ghost fluid method for droplet suspensions under depletion forces

Zhouyang Ge[a,*], Jean-Christophe Loiseau[a,1], Outi Tammisola[a,b], Luca Brandt[a]

[a] *Linné Flow Centre and SeRC (Swedish e-Science Research Centre), KTH Mechanics, S-100 44 Stockholm, Sweden*
[b] *Faculty of Engineering, The University of Nottingham, NG72RD Nottingham, UK*

arXiv:1701.07385v2 [physics.flu-dyn] 1 Feb 2017

Abstract

Aiming for the simulation of colloidal droplets in microfluidic devices, we present here a numerical method for two-fluid systems subject to surface tension and depletion forces among the suspended droplets. The algorithm is based on a fast, second-order-accurate solver for the incompressible two-phase Navier-Stokes equations, and uses a level set method to capture the fluid interface. The four novel ingredients proposed here are, firstly, an interface-correction level set method (iCLS) that efficiently preserves mass. Global mass conservation is achieved by performing an additional advection near the interface, with a correction velocity obtained by locally solving an algebraic equation, which is easy to implement in both 2D and 3D. Secondly, we report a second-order accurate estimation of the curvature at the interface and, thirdly, the combination of the ghost fluid method with the fast pressure-correction approach enabling an accurate and fast computation even for large density contrasts. Finally, we derive a sharp formulation for the pressure difference across the interface induced by depletion of surfactant micelles and combine it with a multiple level-set approach to study short-range interactions among droplets in the presence of attracting forces.

Keywords: Multiphase flow, Level set method, Ghost fluid method, Colloidal droplet

1. Introduction

In the field of colloidal science, much progress has been made on the synthesis of complex building blocks mimicking molecular structures to elaborate innovative materials, *e.g.* materials with complete three dimensional band gaps [1, 2, 3, 4]. The basic elements of such colloidal molecules are particles or droplets less than one millimeter in size, and their self-assembly relies on either lengthy brownian motion or careful microfludic designs, on top of typical colloidal interactions, *e.g.* depletion attraction and electrostatic repulsion [5, 6, 7]. Regardless of the approach, however, questions remain why the colloidal particles/droplets undergo certain path to organize themselves and how

*Corresponding author.
Email addresses: zhoge@mech.kth.se (Zhouyang Ge), jean-christophe.loiseau@ensam.eu (Jean-Christophe Loiseau), outi@mech.kth.se (Outi Tammisola), luca@mech.kth.se (Luca Brandt)
URL: https://github.com/GeZhouyang (Zhouyang Ge)
[1] Present address: Laboratoire DynFluid, Arts et Métiers ParisTech, 151 boulevard de l'hôpital, 75013 Paris, France

such process can be controlled and optimized. Since full data are not yet accurately accessible from experiments in such miniature systems, computer simulations will be useful to provide supplemental information.

Scaling down to microscale appears first to be a convenience for the numerical simulations of multicomponent and multiphase systems as the non-linear Navier-Stokes (NS) equations can be reduced to the linear Stokes equations. This allows the use of boundary integral methods (BIM) [8], *e.g.* most recently the GGEM-based BIM [9, 10] solving the Stokes equations in general geometries. However, it is also possible to use the conventional unsteady, fractional-step/projection-method NS solver at low Reynolds number, combined with an interface description method [11, 12]. The latter approach is more versatile, probably less difficult to implement, and enjoys a rich literature of standard numerical techniques. Here, in view of a rich range of possible applications and considering also the rapid development of inertial microfluidics (where inertial effects are used to better control the flow behavior) we take the approach of simulating the incompressible, two-fluid NS as outlined in [13]. The splitting procedure proposed in [13] enables the use of fast solvers for the pressure Poisson equation also for large density and viscosity contrasts. The remaining choice then is to be made among the available interface-description methods.

Generally, there are two catagories of methods to resolve an interface in the frame of a NS solver, *i.e.* front-tracking methods and front-capturing methods. An example of the front-tracking method is the immersed boundary method (IBM) [14]. It is a Lagrangian-based method, hence it offers a sharp description of the interface. However, for deforming interfaces, these approaches requires frequent mesh rearrangement. Furthermore, topology changes are to be handled manually, making such methods typically more expensive and of limited interest for droplet simulations.

Front-capturing methods, on the other hand, are Eulerian and handle topology changes automatically; they are therefore typically easier to parallelize to achieve higher efficiency. One of such methods is the volume-of-fluid (VOF) method [15], which defines different fluids with a discontinuous color function. The main advantage of VOF is its intrinsic mass conservation property. It suffers however from inaccurate computations of the interface properties, *e.g.* normals and curvatures. This makes it less favorable for simulations of microfluidic systems where surface tension becomes dominant.

Another popular front-capturing method is the level set (LS) method [16, 17]. Contrary to VOF, LS prescribes the interface through a smooth level set function which usually takes the form of the signed distance to the interface. Due to its smoothness, normals and curvatures of the interface can be readily and accurately computed. The problem, nevertheless, is that mass loss/gain may occur and accumulate because of numerical diffusion in the solution of the LS transport and because of the errors introduced in a procedure called reinitialization, commonly required to reshape the level set into a distance function. Therefore, additional measures have to be taken to fix this problem.

Many different approaches have been proposed to make LS conservative, which can be classified into the following three methodologies. The first is to improve the level set discretization and reinitialization, so that numerical errors are reduced. In practice, one can increase the order of level set fluxes [18], minimize the displacement of the zero level set during reinitialization [19, 18], or employ local mesh refinement [20]. By doing so, mass loss can be greatly reduced, although the formulation is still inherently non-conservative. The second remedy couples the LS with the VOF, *e.g.* the so-called CLSVOF methods

[21], MCLS [22], or the most recent curvature-based mass-redistribution method [23]. With varying level of coupling, these methods can usually preserve mass equally well as VOF; yet the complexity and some inaccuracy of VOF will be imported, making it less elegant. The third approach to guarantee mass conservation is to modify the the formulation of the LS, or the LS or NS equations, so that LS becomes globally mass-conserving. Examples of this kind include the hyperbolic-tangent level set [24], the extension-velocity level set [25], and the mass-preserving NS projection method [26]. Such approaches are conceptually simple and can lead to good mass conservation; however, they may also result in unphysical numerical artifacts or have limited applications.

With the physical background of colloidal droplets in mind, and partially inspired by the mass-preserving NS projection method [26], we propose a simple interface-correction level set (iCLS) method. The idea is to obtain a normal velocity field at the droplet interface and use it to perform an additional advection of the LS function to compensate for mass loss, in a way similar to inflating a balloon. Because no coupling with VOF is required, the simplicity and high accuracy of the original LS method is preserved, yet the extra computational cost of this procedure is negligible.

Based on the newly proposed iCLS method, we extend the single level set (SLS) function to multiple level sets (MLS). MLS has the benefits that each droplet can be treated individually, is allowed to interact with the other droplets and is guarded from its own mass loss. MLS also prevents numerical coalescence of droplets when they get close. The computational cost of MLS is proportional to the number of droplets and the number of total cells, *i.e.* $\mathcal{O}(lN^2)$ in 2D or $\mathcal{O}(lN^3)$ in 3D, with l being the number of droplets and N being the number of cells in each dimension. With a simple narrow band approach, this cost can be roughly reduced to $\mathcal{O}(lN)$ and $\mathcal{O}(lN^2)$, respectively.

One difficulty of the simulation of multiphase flow is the presence of surface tension, which manifests itself as a pressure jump across an infinitesimally thin interface. In microfluidic systems, particularly, surface tension becomes more prominent since it scales linearly with the dimension of the system (hence diminishes slower than volumetric forces such as gravity). To handle this discontinuity, the most widely-adopted approach is the continuum surface force (CSF) [27], which smears out the density contrast and models the surface tension as a smoothed forcing term near the interface. CSF effectively introduces an artificial spreading of the interface and is prone to errors when two interfaces are within its smoothing width.

Another interesting technique, in the context of finite-difference discretizations of the NS equations, is the ghost fluid method (GFM). It was originally devised to keep a sharp density profile in the compressible Euler equations [28], but has later been extended to treat the normal stress discontinuities in incompressible NS equations [**?**]. As shown by Desjardins *et al* [30], using GFM for the pressure jump due to surface tension and neglecting the normal jump due to viscosity difference result in a second-order accurate pressure field, while preserving the discontinuity for both pressure and density. Their original algorithm is framed for solving the pressure Poisson equation iteratively, *e.g.* through a multi-grid solver. Here, we first propose a second-order accurate, grid-converging interface curvature estimation, and then adapt it to a fast pressure-correction method (FastP*) [13] that benefits from an efficient, FFT-based, direct solver. The only additional requirement from [13] is that the computational domain is periodic in at least two directions.

Finally, an unique challenge to the simulation of colloidal droplets is the modeling of

near-field interactions. It is known that two or more colloids can interact via dispersion, surface, depletion, and hydrodynamic forces [5]. Apart from the hydrodynamic forces, which can be determined from the NS solver directly, and the dispersion forces, which arise from quantum mechanical effects, the depletion and surface forces have to be modeled. These forces can be either attraction or repulsion and are typically calculated from the gradient of a potential. Hence, MLS is needed to determine the interaction forces. Combining with GFM, we propose a novel method to compute the near field interactions in our NS solver. The GFM makes the interaction force sharp and the MLS makes it possible for two droplets to be closer than one grid cell without automatic merging.

The paper is organized as follows. In Sec. 2, the governing equations for the incompressible, two-phase flow are briefly presented. We then describe in Sec. 3, the classical signed-distance level set methodology and the numerical methods adopted. In sec. 4, we propose an interface-correction level set method that is mass-conserving. In Sec. 5, we derive an interface curvature estimation and demonstrate its second-order convergence. Our coupled flow solver is outlined in Sec. 6 along with three validation cases. Finally, we propose a MLS/GFM-based method for the modeling of near-field depletion potential in Sec. 7.

2. Governing equations for interfacial two-phase flow

The dynamics of the incompressible flow of two immiscible fluids is governed by the Navier-Stokes equations, written in the non-dimensional form

$$\nabla \cdot \mathbf{u} = 0, \tag{1a}$$

$$\frac{\partial \mathbf{u}}{\partial t} + \mathbf{u} \cdot \nabla \mathbf{u} = \frac{1}{\rho_i}\bigg(- \nabla p + \frac{1}{Re}\nabla \cdot \big[\mu_i(\nabla \mathbf{u} + \nabla \mathbf{u}^T)\big]\bigg) + \frac{1}{Fr}\mathbf{g}, \tag{1b}$$

where $\mathbf{u} = \mathbf{u}(\mathbf{x}, t)$ is the velocity field, $p = p(\mathbf{x}, t)$ is the pressure field, and $\mathbf{g}$ is a unit vector aligned with gravity or buoyancy. ρ_i and μ_i are the density and dynamic viscosity ratios of fluid i ($i = 1$ or 2) and the reference fluid. These properties are subject to a jump across the interface, which we denote as $[\rho]_\Gamma = \rho_2 - \rho_1$ for density and $[\mu]_\Gamma = \mu_2 - \mu_1$ for viscosity. For viscous flows, the velocity and its tangential derivatives are continuous on the interface [31]. However, the pressure is discontinuous due to the surface tension and the viscosity jump, *i.e.*

$$[p]_\Gamma = \frac{1}{We}\kappa + \frac{2}{Re}[\mu]_\Gamma \mathbf{n}^T \cdot \nabla \mathbf{u} \cdot \mathbf{n}, \tag{2}$$

where κ is the interface curvature, and $\mathbf{n}$ is the normal to the interface. If the surface tension coefficient, $\tilde{\sigma}$, varies on the interface the tangential stress is also discontinuous. In this paper, we assume constant and uniform $\tilde{\sigma}$. In Eqs. (1b) and (2), Re, We, and Fr are, respectively, the Reynolds, Weber, and Froude numbers, defined as

$$Re = \frac{\tilde{\rho_1}\tilde{U}\tilde{L}}{\tilde{\mu_1}}, \qquad We = \frac{\tilde{\rho_1}\tilde{U}^2\tilde{L}}{\tilde{\sigma}}, \qquad Fr = \frac{\tilde{U}^2}{\tilde{g}\tilde{L}}, \tag{3}$$

where $\tilde{U}$, $\tilde{L}$, $\tilde{\rho_1}$, $\tilde{\mu_1}$, and $\tilde{g}$ denote the reference dimensional velocity, length, density, dynamic viscosity, and gravitational acceleration. Note that $\rho_1 = 1$ and $\mu_1 = 1$ (i.e. we define fluid 1 as the reference fluid).

3. Classical level set methodology

In the level set framework, the interface Γ is defined implicitly as the zero value of a scalar function $\phi(\mathbf{x}, t)$, *i.e.* $\Gamma = \{\mathbf{x} \mid \phi(\mathbf{x}, t) = 0\}$. Mathematically, $\phi(\mathbf{x}, t)$ can be any smooth or non-smooth function; but it is classically shaped as the signed distance to the interface [32, 17], *viz.*

$$\phi(\mathbf{x}, t) = sgn(\mathbf{x})|\mathbf{x} - \mathbf{x}_{\mathbf{\Gamma}}|, \tag{4}$$

where $\mathbf{x}_{\mathbf{\Gamma}}$ denotes the closest point on the interface from nodal point $\mathbf{x}$, and $sgn(\mathbf{x})$ is a sign function equal to 1 or -1 depending on which side of the interface it lies. For two-fluid problems with single level set, $sgn(\mathbf{x})$ provides a natural "color function" for phase indication. Furthermore, with this definition, geometric properties such as the unit normal vector, $\mathbf{n}$, and the local mean curvature, κ, can be conveniently computed as

$$\mathbf{n} = \frac{\nabla\phi}{|\nabla\phi|}, \tag{5}$$

$$\kappa = -\nabla \cdot \mathbf{n}. \tag{6}$$

3.1. Advection

The motion of a fluid interface is governed by the following hyperbolic equation

$$\frac{\partial\phi}{\partial t} + \mathbf{u} \cdot \nabla\phi = 0, \tag{7}$$

where $\mathbf{u}$ is the flow velocity field. Despite of its simple form, obtaining an accurate and robust solution to Eq. (7) is challenging. For two-fluid problems, state-of-the-art level set transport schemes include the high-order upstream-central (HOUC) scheme [18], the weighted essentially non-oscillatory (WENO) scheme [31], the semi-Lagrangian scheme [33], or the semi-jet scheme [34]. Quantitative comparisons of these schemes in various test cases can be found in [18, 34]. We note that the choice of the scheme is case-dependent, *i.e.* depending on the smoothness of the overall level set field or the stiffness of Eq. (7). For flows involving moderate deformations, HOUC is usually sufficient and most efficient. For more complex flows, WENO or semi-Lagragian/jet schemes combined with subcell resolution might be pursed. In the present study, we use either HOUC5 or WENO5 (5 denotes fifth-order accuracy) to evaluate $\nabla\phi$.

For the temporal discretization of Eq. (7), we use a three-stage total-variation-diminishing (TVD) third-order Runge-Kutta scheme [35]. At each time step Δt, it updates ϕ from time level n to $n+1$ in three sub-steps

$$\begin{cases} \phi^1 = \phi^n + \Delta t \cdot f(\phi^n) \\ \phi^2 = \frac{3}{4}\phi^n + \frac{1}{4}\phi^1 + \frac{1}{4}\Delta t \cdot f(\phi^1) \\ \phi^{n+1} = \frac{1}{3}\phi^n + \frac{2}{3}\phi^2 + \frac{2}{3}\Delta t \cdot f(\phi^2) \end{cases} \tag{8}$$

where $f(\phi) = -\mathbf{u} \cdot \nabla\phi$.

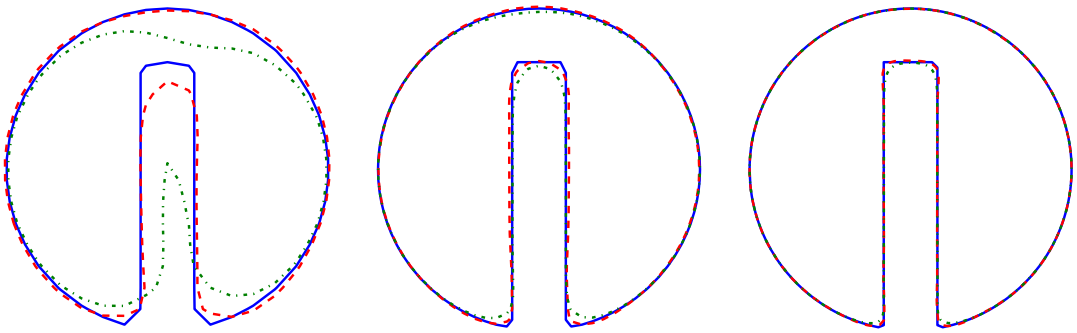

(a) 50×50 (b) 100×100 (c) 200×200

Figure 1: Comparison of the initial interface and its shape after one full rotation for different mesh resolutions. Solid lines depict the initial interface. Two different schemes have been used to evaluate the gradients, namely HOUC5 (dashed lines) and WENO5 (dash-dotted line).

Zalesak's disk. The Zalesak's disk [36], *i.e.* a slotted disc undergoing solid body rotation, is a standard benchmark to validate level set solvers. The difficulty of this test lies in the transport of the sharp corners and the thin slot, especially in under-resolved cases. The initial shape should not deform under solid body rotation. Hence, by comparing the initial level set field and that after one full rotation one can characterise the degree of accuracy and mass conservation of a numerical solver. Here, the parameters are chosen so that a disk of radius 0.15, slot width of 0.05 is centered at $(x, y) = (0, 0.25)$ of a $[-0.5, 0.5] \times [-0.5, 0.5]$ box. The constant velocity field is given as

$$u = -2\pi y, \quad v = 2\pi x. \tag{9}$$

Three different mesh resolutions have been considered, namely 50×50, 100×100 and 200×200. Fig. 1 depicts the shape of the interface after one full rotation of the disk for the different meshes. Along with the results of the HOUC5 scheme (red dashed line), the shape of the interface obtained using the WENO5 scheme (green dash-dotted line) is also reported on this figure. Both schemes yield good results on fine grids, but the HOUC5 scheme clearly outperforms the WENO5 scheme on the coarsest mesh considered here.

3.2. Reinitialization

Although the level set function is initialized to be a signed-distance function, it may lose this property as time evolves. This can cause numerical issues, particularly in the evaluation of the normals $\mathbf{n}$ and curvature κ [17]. In order to circumvent these problems, an additional treatment has to be introduced to reshape ϕ into a distance function, as in Eq. (4). There are mainly two approaches to enforce Eq. (4), either with a direct, fast marching method (FMM) [16], or converting it into a time-dependent Hamilton-Jacobi equation [17]

$$\frac{\partial \phi}{\partial \tau} + S(\phi_0)(|\nabla \phi| - 1) = 0 \tag{10}$$

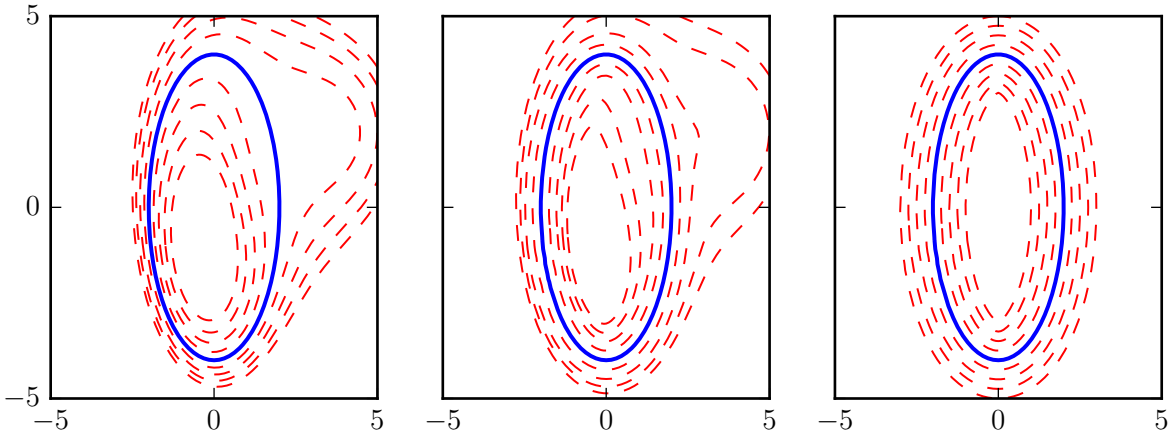

(a) Initial condition (b) After 25 steps (c) After 100 steps

Figure 2: Illustration of the reinitialization procedure. The shape of the ellipsoid is depicted as the thick solid line. The dashed lines then depict iso-contours of $\phi(x, y)$ ranging from -1 to 1 by increments of 0.25.

where τ is a pseudo-time, and $S(\phi_0)$ is a mollified sign function of the original level set, defined as

$$S(\phi_0) = \begin{cases} -1 & \text{if} \quad \phi_0 < -\Delta x \\ 1 & \text{if} \quad \phi_0 > \Delta x \\ \frac{\phi_0}{\sqrt{\phi_0^2 + \Delta x^2}} & \text{otherwise.} \end{cases} \tag{11}$$

The first approach is more complicated to implement and is typically at best second-order accurate. Here, we take the second approach. Specifically, we use the SSP-RK3 scheme for time integration, and WENO5 to evaluate the spatial derivatives.

Distorted elliptic field. In order to illustrate the redistancing procedure, a test case similar to the one by Russo and Smereka [37] is considered. Let us define the initial level set field as

$$\phi(x, y, 0) = f(x, y) \left(\sqrt{\left(\frac{x^2}{4} + \frac{y^2}{16} \right)} - 1 \right)$$

with $f(x, y)$ a distortion function that leaves only the location of the interface unchanged. The initial condition is displayed in Fig. 2(a), where the shape of the ellipse is depicted as the thick blue line. The red dashed lines depict iso-contours of $\phi(x, y)$ ranging from -1 to 1. Clearly, this initial condition is far from being a distance function, the iso-contours not being equidistant. As the function ϕ is evolved under Eq. (10), it slowly converges towards a signed-distance function as can be assessed from Fig. 2(b) and (c). From a practical point of view, it has to be noted that, provided the initial condition $\phi(x, y, 0)$ is close enough to a distance function, then very few iterations of the reinitialization Eq. (10) are required for ϕ to be transformed back into a signed-distance function. Typically, one iteration every ten to a hundred time steps is sufficient to reshape ϕ, see *e.g.* discussions in [38]. Therefore, the computational cost of the reinitialization step is usually negligible.

3.3. Narrow band approach

The level set methodology introduced so far applies to the whole computational domain. In fact, for multiphase-flow problems, only the local level set values adjacent the interface are important. This has motivated the development of the so called narrow band methods, which can reduce the operation counts from $\mathcal{O}(N^2)$ (2D) or $\mathcal{O}(N^3)$ (3D) to roughly $\mathcal{O}(N)$ or $\mathcal{O}(N^2)$, with N being the number of points in one dimension; see *e.g.* [39, 40]. Here, we implement a similar narrow band approach as in [40], in which the level set advection and reinitialization are solved within a short tube surrounding the interface. In the original algorithm, a cut-off function $c(\phi)$ is applied to the advection equation $\phi_t + c(\phi)\mathbf{u}\cdot\nabla\phi = 0$ to avoid numerical oscillations propagating from the boundary of the narrow band. The cut-off function, based on ENO or WENO schemes, includes a smooth transition from the inner tube to the outer tube. For the HOUC5 scheme, among all the tests we have done, we find that a simple step function will work, *i.e.*

$$c(\phi) = \begin{cases} 1 & \text{if} \quad \phi < \gamma \\ 0 & \text{otherwise} \end{cases} \tag{12}$$

where γ is the distance from the edge of the narrow band to the interface. Note that γ needs to be sufficiently large that the stencil of spatial discretization scheme lies totally within it. For both HOUC5 and WENO5, the minimal value of γ is $3\Delta x$. In the current work, $\gamma = 8\Delta x$ is used to provide the additional information required to model droplet interactions (Sec. 7).

4. Interface-correction level set (iCLS) method

It is known that classical level set methods lead to mass loss when applied to multiphase flows, partially because there is no underlying mass conservation in the level set formalism, partially because of the reinitialization procedure. Such errors can be reduced or even removed by using elaborated schemes [20] or coupling with VOF [21, 23]. However, doing so often makes the level set schemes complicated to implement and less efficient. To maintain the simplicity of the original level set method, we propose the alternative approach to conserve mass by performing small corrections near the interface. Because such corrections are done by directly solving a PDE (same as Eq. (7)), the proposed method is straightforward to implement in both 2D and 3D. Meanwhile, because the correction does not need to be performed at every time step, the additional cost is negligible. Below, we first present the derivation of the correction, then we demonstrate the mass conservation with an example.

Let Γ divide a domain into two disjoint subsets Ω_1 (*e.g.* a droplet) and Ω_2 (*e.g.* the ambient fluid), and V denote the volume of Ω_1. Without loss of generality, we let $\phi < 0$ in Ω_1, and $\phi > 0$ in Ω_2. The rate of change of V can be written as the integral of a normal velocity, $\mathbf{u}_c$, defined on Γ [26], *i.e.*

$$\int_\Gamma \mathbf{n}\cdot\mathbf{u}_c \, d\Gamma = \frac{\delta V}{\delta t}, \tag{13}$$

where $\mathbf{n}$ is the outward-pointing normal from the interface Γ. If $-\delta V/\delta t$ corresponds to the mass loss over an arbitrary period of time (it does not have to be the time step of the level set advection), then $\mathbf{u}_c$ can be thought as a surface velocity that corrects the

volume by an amount $\delta V/\delta t$, hence compensating the mass loss. In other words, if $\mathbf{u}_c$ is known, then the following PDE can be solved,

$$\frac{\partial \phi}{\partial t} + \mathbf{u}_c \cdot \nabla \phi = 0, \tag{14}$$

after which the mass loss accumulated over δt is removed.

To obtain such a surface correction-velocity $\mathbf{u}_c$, we introduce a speed function, f_s, an auxiliary variable, p_c, and express the rate of change of $\mathbf{u}_c$ as

$$\frac{d\mathbf{u}_c}{dt} = -f_s \nabla p_c. \tag{15}$$

Here, p_c can be seen as a non-dimensional correction-pressure in Ω_1. If $f_s = 1$, the physical interpretation of Eq. (15) is to inflate or deflate a balloon by δV with pressure p_c over Δt (see Fig. 3). This is more evident when we recast it in the form of the impulse-momentum theorem (per unit "mass" of the interface)

$$\mathbf{u}_c = -\int_0^{\Delta t} \nabla p_c \, dt, \tag{16}$$

in which the correction-velocity is zero at $t = 0$, and we require $f_s \equiv 1$.

For a general choice of f_s, we may substitute Eq. (16) into Eq. (13) which results in

$$\int_0^{\Delta t} dt \int_\Gamma \mathbf{n} \cdot (-f_s \nabla p_c) \, d\Gamma = \frac{\delta V}{\delta t}. \tag{17}$$

In order for ∇p_c to be compatible with $\mathbf{u}_c$, p_c has to be differentiated at the interface. This turns out to be easy in the level set framework, as we can use a 1D regularized Heaviside function of ϕ, such as

$$H_\epsilon(\phi) = \begin{cases} 1 & \text{if} \quad \phi > \epsilon \\ \frac{1}{2}\big[1 + \frac{\phi}{\epsilon} + \frac{1}{\pi}\sin(\frac{\pi\phi}{\epsilon})\big] & \text{if} \quad |\phi| \leqslant \epsilon \\ 0 & \text{otherwise,} \end{cases} \tag{18}$$

with $\epsilon = 1.5\Delta x$ being the half smoothing width. This way, the correction-pressure and its gradient in Eq. (17) can be conveniently written as

$$p_c = \big(1 - H_\epsilon(\phi)\big) p_0, \tag{19}$$

and

$$\int \nabla p_c = -\int \delta_\epsilon(\phi) \nabla \phi p_0, \tag{20}$$

where $\delta_\epsilon(\phi)$ is the derivative of $H_\epsilon(\phi)$, and p_0 is a constant. Noting that $\mathbf{n} \cdot \nabla \phi = |\nabla \phi| = 1$ for a distance level set function, and denoting $\int_\Gamma f_s \delta_\epsilon(\phi) \, d\Gamma = A_f$, we arrive at a simple, explicit expression for the constant pressure

$$p_0 = \frac{\delta V}{\delta t} \frac{1}{A_f \Delta t}, \tag{21}$$

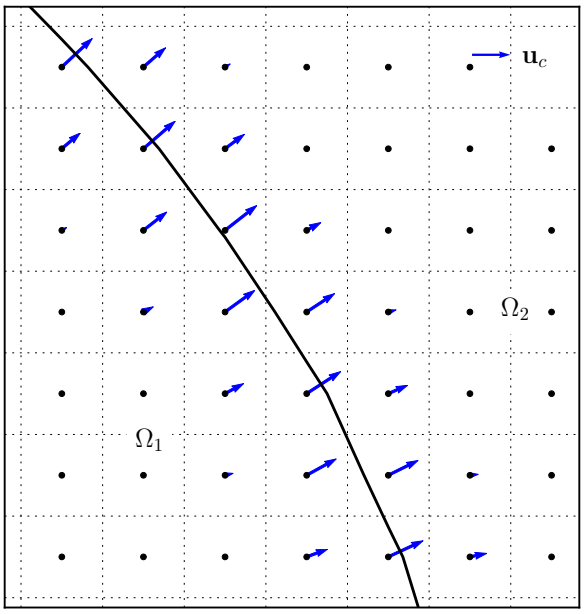

Figure 3: 2D illustration of the mass correction. The solid line represents the interface. The arrows indicate the normal correction-velocity located at cell centers of the grid.

in which we have made a first-order approximation for the time integration in Eq. (16), *i.e.* $\int_0^{\Delta t} A_f \, dt = A_f \Delta t$. Finally, from Eqs. (15) (20) and (21), the correction-velocity can be written as

$$\mathbf{u}_c(\phi) = \frac{\delta V}{\delta t} \frac{f_s \delta_\epsilon(\phi)}{A_f} \nabla \phi, \tag{22}$$

or

$$\mathbf{u}_c(\phi) = \frac{\delta V}{\delta t} \frac{f_s}{A_f} \nabla H_\epsilon(\phi). \tag{23}$$

Eq. (22) or (23) gives an expression for the surface correction-velocity in Eq. (14). Here, we have required a bounded support for $\mathbf{u}_c$, *i.e.* $\mathbf{u}_c = \mathbf{0}$ for $|\phi| \geqslant \epsilon$. There are two benefits of spreading the surface velocity. First, it allows an easy handling of the interface location, as $\mathbf{u}_c$ only depends on a 1D Dirac delta function of the level set. The choice of $\delta_\epsilon(\phi)$ can also be different from the trigonometric form in Eq. (18), *e.g.* one can use the linear hat in [41]. The important point is that we spread the *correction-velocity* rather than the *interface*. The interface remains sharp, as it is implicitly represented by the level set function. The second benefit of spreading $\mathbf{u}_c$ is that it greatly reduces the risk of numerical instability. As $\mathbf{u}_c$ is supported on a 2ϵ band around the interface, the maximal nodal value of $\mathbf{u}_c$ scales with $1/\epsilon$. In our tests, we have never found its non-dimensional value to exceed 1. Therefore, the CFL conditions imposed by Eq. (14) is always satisfied as long as we use the same temporal scheme (*e.g.* RK3) for solving Eq. (7) and Eq. (14).

In Eq. (22) or (23), $\mathbf{u}_c$ is written as a function of ϕ only. The speed function, f_s, introduced in Eq. (15), acts as a pre-factor for $\mathbf{u}_c$. Specifically, we can define it in two

ways

$$f_s \equiv \begin{cases} 1 & \text{uniform speed} \\ \kappa(\phi) & \text{curvature-dependent speed.} \end{cases} \tag{24}$$

The uniform speed will thus result in a fixed strength, $\frac{\delta V}{A(\phi)\delta t}$, for the velocity distribution. In the case of a static spherical droplet, this is the ideal choice for f_s, since the droplet should remain a sphere. In more general cases, when a fluid interface is subject to deformations or topological changes, a curvature-dependent speed may be more appropriate. This is based on the assumption that local structures of higher curvature are more prone to mass losses, and indeed a linear curvature weight has been demonstrated to produce accurate results [23]. Furthermore, κ/A_f reduces to $1/A_f$ when the curvature is uniform. Therefore, we can rewrite Eq. (23) for a curvature-dependent speed as

$$\mathbf{u}_c(\phi) = \frac{\delta V}{\delta t}\frac{\kappa(\phi)}{A_f}\nabla H_\epsilon(\phi). \tag{25}$$

Clearly, the velocity $\mathbf{u}_c$ resulting from Eq. (25) is larger in highly curved parts, and smaller in flatter parts. It thus includes "local" information while maintaining "global" mass conservation. Standard central-difference discretization applies, where the components of $\mathbf{u}_c$ can be obtained at either the cell faces or cell centers. The computation of $\kappa(\phi)$ is crucial and will be presented in the next section. We also note that such a curvature-dependency is not unique. In principle, one can choose different weight-functions based on specific conditions. Practically, the difference is expected to be negligible since the mass loss remains small (typically around 10^{-5}) at each correction step.

After correcting the level set near the interface with Eq. (14), a reinitialization step is required to redistance the whole level set field within its narrow band. The two procedures can be readily combined, since it is not necessary to perform mass correction at every time step. Because the whole formalism is cast in a level set frame, generalization from 2D to 3D is trivial. The additional computational cost is negligible, as it only involves solving one PDE directly; whereas a typical VOF-coupling method will require solving another set of transport equations [21], or reconstructing the interface by an iterative procedure [23].

In summary, the iCLS method proceeds by performing the following steps:

1. Advect ϕ^n from time t^n to t^{n+1} with Eq. (7), using the flow velocity $\mathbf{u}^n$.
2. If reinitialization will be executed (otherwise, go to step 3):
   (a) Perform mass correction using $\mathbf{u}_c$ from Eq. (25).
   (b) Reinitialize ϕ^{n+1} with Eq. (10).
3. Exit the LS solver.

Deforming circle. The deformation of a circle by a single vortex is a standard test case to assess the ability of numerical methods to resolve thin filaments. In a $[0,1]\times[0,1]$ box, a circle of radius 0.15 is initially centered at $(0.5, 0.75)$. The velocity is derived from the stream function

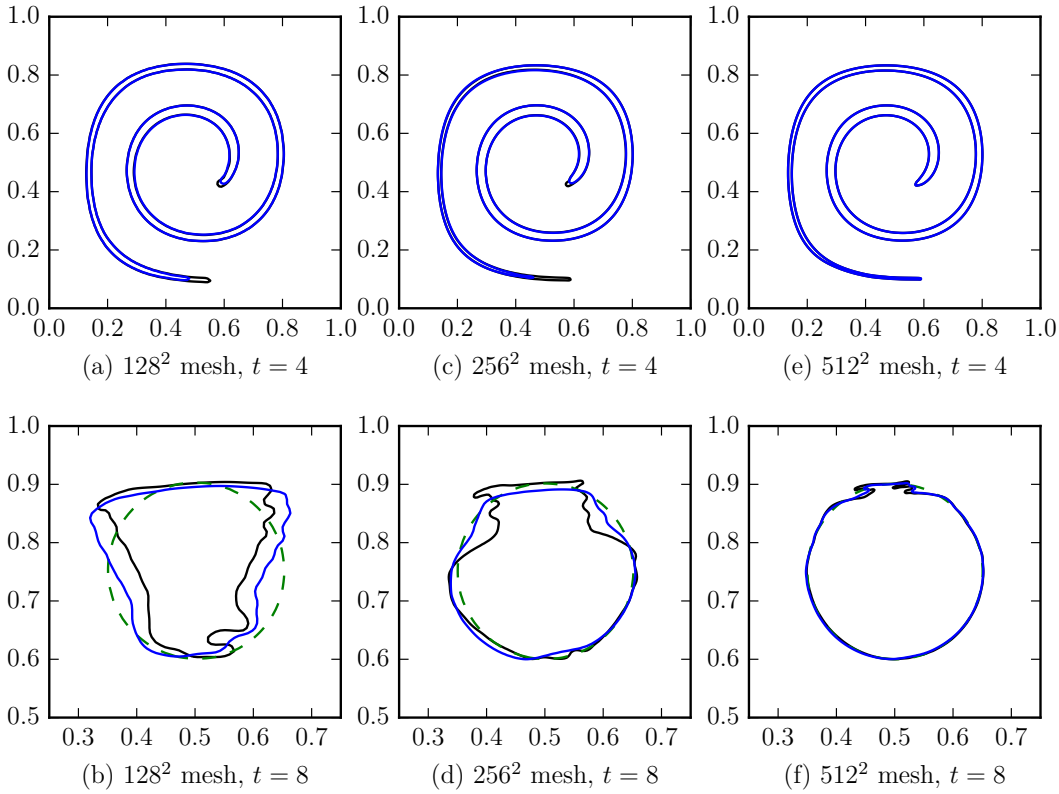

(a) 128^2 mesh, $t = 4$ (c) 256^2 mesh, $t = 4$ (e) 512^2 mesh, $t = 4$

(b) 128^2 mesh, $t = 8$ (d) 256^2 mesh, $t = 8$ (f) 512^2 mesh, $t = 8$

Figure 4: Interface at $t = 4$ and $t = 8$ for different meshes. The solid black lines indicate simulations without mass correction, the solid blue lines indicate simulations with the current mass correction method, the green dashed lines in (b)(d)(f) indicate the original circle. (For interpretation of the references to color in this figure legend, the reader is referred to the web version of this article.)

$$\psi(x, y, t) = \frac{1}{\pi} \sin^2(\pi x) \cos^2(\pi y) \cos\left(\frac{\pi t}{T}\right),$$

where T is traditionally set to 8. The deformation of the circle will be maximum at time $t = T/2$, and the process is then inverted until time $t = T$, when the circle should be back to its initial location and shape.

Fig. 4 shows the shape of the filament/circle at $t = 4$ and $t = 8$ for different meshes with our level set solver. With mass correction, the filament has a smoother tail and head at the time of maximal stretch, and finally returns closer to its initial circular shape, than to without mass correction. As we increase the resolution significantly, the difference in the final shape becomes smaller. The improvement in mass conservation is very clear from the curves in Fig. 5.

5. Curvature computation

5.1. Cell-center curvature

Curvature computation is crucial to interfacial flows in the presence of surface tension [20, 30], and even more so in our case, when we apply curvature-dependent interface

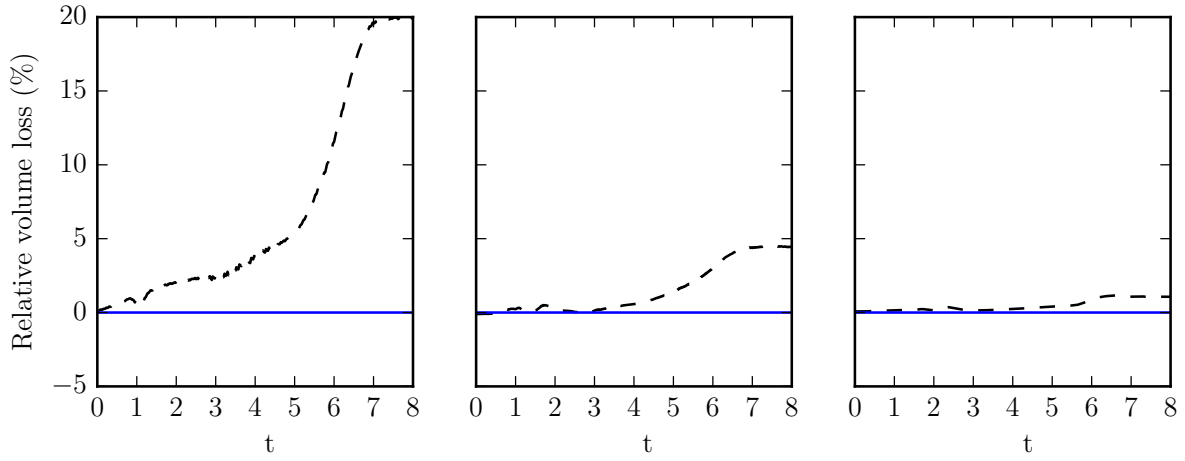

(a) 128^2 mesh (b) 256^2 mesh (c) 512^2 mesh

Figure 5: Relative volume loss for three different meshes. Dashed lines indicate simulations without mass correction; solid lines indicate simulations with mass correction.

corrections. Inaccurate curvature can result in unphysical spurious currents, as will be shown in Sec. 6.5.1. From Eq. (6), the curvature κ can be evaluated as

$$\kappa = -\frac{\phi_{yy}\phi_x^2 + \phi_{xx}\phi_y^2 - 2\phi_x\phi_y\phi_{xy}}{\left(\phi_x^2 + \phi_y^2\right)^{3/2}} \tag{26}$$

and as

$$\kappa_M = -\frac{\left\{\begin{array}{r}(\phi_{yy} + \phi_{zz})\phi_x^2 + (\phi_{xx} + \phi_{zz})\phi_y^2 + (\phi_{xx} + \phi_{yy})\phi_z^2 \\ -2\phi_x\phi_y\phi_{xy} - 2\phi_x\phi_z\phi_{xz} - 2\phi_y\phi_z\phi_{yz}\end{array}\right\}}{\left(\phi_x^2 + \phi_y^2 + \phi_z^2\right)^{3/2}} \tag{27}$$

in 2D and 3D Cartesian coordinates, respectively, where the subscript M denotes the mean curvature [16]. The curvature can be determined from these expressions using simple central finite-differences. It has to be noted, however, that such evaluation of κ involves second derivatives of the level set field $\phi(\mathbf{x})$. As a consequence, if the discretization of ϕ is only second-order accurate, the resulting κ will be of order zero [30]. To nonetheless retain a grid converging κ, one can use the compact least-squares scheme proposed by Marchandise *et al* [42]. Their approach provides a second-order, grid converging evaluation of the cell-center curvature. It moreover smears out undesired high frequency oscillations possibly introduced by the velocity field. A similar procedure has also been adopted in other works [30, 23].

The principle of the least squares approach is to solve an overdetermined linear system, $\mathbf{Ax} = \mathbf{b}$, where $\mathbf{A}$ is a matrix built from the local coordinates, $\mathbf{x}$ is a unknown array containing the reconstructed level set values and its spatial derivatives, and $\mathbf{b}$ is the original level set field. The detailed descriptions can be found in [42]. Here, we only note that the level set function remains unmodified after this step. From a practical point of view, provided the mesh considered is uniform in all directions, the pseudoinverse of the

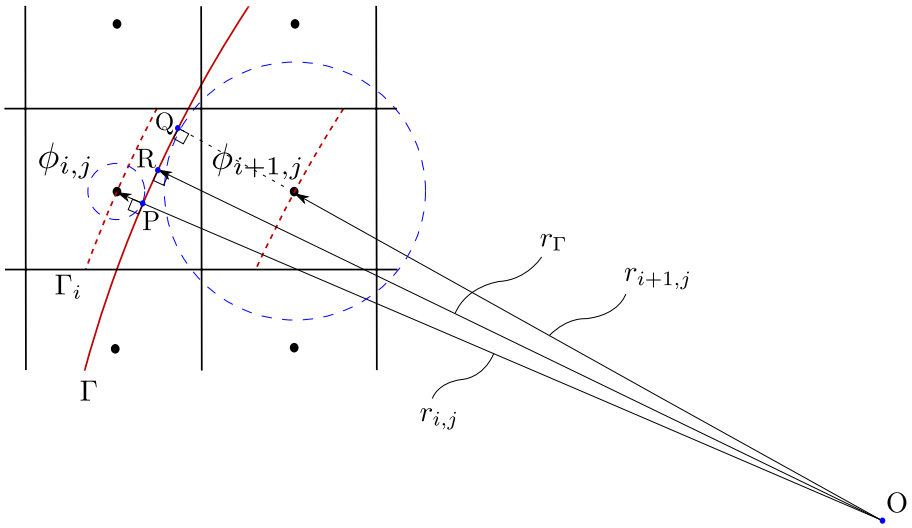

Figure 6: Estimation of the interface's curvature from neighboring cells.

matrix $\mathbf{A}$ only needs to be evaluated once and applied close to the interface. Therefore, the computational cost of this least-squares calculation is negligible.

5.2. Interface curvature

The least-squares approach described in the previous section only allows one to compute the nodal curvature κ of the level set field ϕ. For computations using the GFM (Sec. 6.2), one might however require an accurate evaluation of the curvature at the exact location of the interface. Provided a grid-converging cell-center curvature, the actual curvature at the interface can be interpolated from its neighboring cells weighted by the level set [43, 44]. Here we present a slightly different but robust algorithm to estimate the interface curvature, with a straight-forward geometrical interpretation.

2D estimation. Suppose the interface Γ cuts through two adjacent cells, (i, j) and $(i+1, j)$, where the cell-center curvatures $\kappa_{i,j}$ and $\kappa_{i+1,j}$ are known. In 2D, we can determine the radius of curvature at each cell directly from

$$\kappa_{i,j} = -\frac{1}{r_{i,j}}, \qquad \kappa_{i+1,j} = -\frac{1}{r_{i+1,j}}, \tag{28}$$

as illustrated in Fig. 6. Since the level set is defined as the signed distance to the interface, Γ must be tangent to a circle of radius $|\phi_{i,j}|$ centered at (i, j), and parallel to the contour line of $\Gamma_i = \{\mathbf{x}|\phi = \phi_{i,j}\}$ (otherwise they will not remain equidistant). We also know Γ lies between (i, j) and $(i+1, j)$, then it must pass through P (see Fig. 6). Since Γ and Γ_i are parallel and there is only one line normal to both curves passing through P, $r_{i,j}$ and OP must originate from the same point, O. Then we get

$$|OP| = r_{i,j} - s_\Gamma \phi_{i,j}. \tag{29}$$

where s_Γ is a sign function equal to 1 if the interface wrapping the negative level set is convex, and equal to -1 if concave.

The same argument holds for cell $(i+1, j)$, which yields $|OQ| = r_{i+1,j} - s_\Gamma \phi_{i+1,j}$. We can therefore write the radius of the interface curvature between (i, j) and $(i+1, j)$ as

$$r_\Gamma = \frac{|OP| + |OQ|}{2}, \tag{30}$$

so that the interface curvature becomes

$$\kappa_\Gamma = \frac{2}{\kappa_{i,j}^{-1} + \kappa_{i+1,j}^{-1} + s_\Gamma(\phi_{i,j} + \phi_{i+1,j})}. \tag{31}$$

The above derivation provides a relation between the interface curvature and that at the adjacent cell-centers in the x direction. Similar results can be obtained in the y direction (*e.g.* between $\phi_{i,j}$ and $\phi_{i,j-1}$). The assumptions we have made here are 1) the cell-center curvatures are accurate and 2) the interface curvatures at P and Q are the same, so that OP and OQ are co-centered (or, $|OP| \approx |OQ| \approx |OR|$). The second assumption is essentially a sub-cell approximation, and we expect it to be valid as long as the interface is well-resolved. One exception we have found is when two interfaces are closer than about $2\Delta x$, the local level set field will develop "corners". In that case, the cell-center curvatures are erroneous and the underlying assumptions we require here are not fulfilled. We do not discuss that case in the present paper. However, we demonstrate in the next section that a second-order converge is achieved when the interface is resolved.

3D estimation. In three dimensions, the mean curvature of a surface can be written as

$$\kappa_\Gamma = -(\frac{1}{r_{\Gamma 1}} + \frac{1}{r_{\Gamma 2}}), \tag{32}$$

where $r_{\Gamma 1}$ and $r_{\Gamma 2}$ are the two principal radii corresponding to the maximal and minimal planar radius of curvature. Note that here we do not need to approximate the interface as a sphere since there is always a plane where the previous picture (Fig. 6) holds. Under the same assumption as for the 2D case, that the interface at P and Q have the same principal radii (hence the same curvature), one can again relate the nodal curvatures to their nearby interface as

$$\begin{aligned} \kappa_{i,j,k} &= -(\frac{1}{r_{\Gamma 1} + s_\Gamma \phi_{i,j,k}} + \frac{1}{r_{\Gamma 2} + s_\Gamma \phi_{i,j,k}}), \\ \kappa_{i+1,j,k} &= -(\frac{1}{r_{\Gamma 1} + s_\Gamma \phi_{i+1,j,k}} + \frac{1}{r_{\Gamma 2} + s_\Gamma \phi_{i+1,j,k}}), \end{aligned} \tag{33}$$

where s_Γ is the same sign function defined for the 2D case. Comparing equations (32) and (33), it is natural to expand Eq. (33) into a Taylor series and to approximate the interface curvature directly as

$$\kappa_\Gamma = \frac{\epsilon_{i+1}\kappa_i - \epsilon_i \kappa_{i+1}}{\epsilon_{i+1} - \epsilon_i} + O(\epsilon_i^2, \epsilon_{i+1}^2), \tag{34}$$

where

$$\epsilon_i = s_\Gamma \phi_{i,j,k}. \tag{35}$$

Since the level set must change sign across the interface, Eq. (34) is always defined and it reduces to the exact value if the cell center happens to be on the interface. Finally,

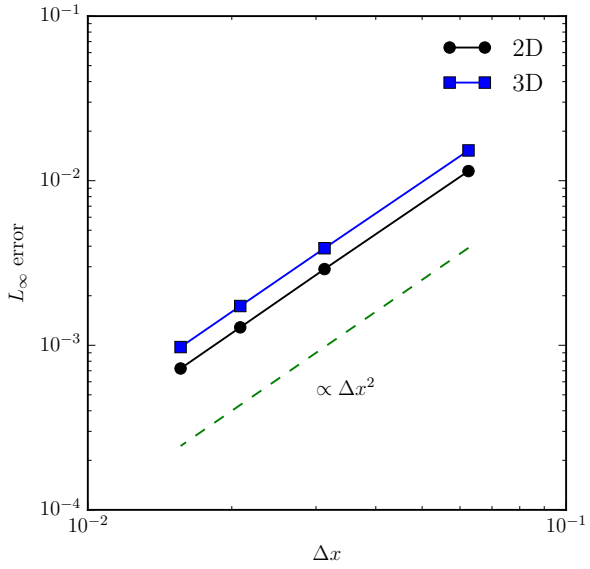

Figure 7: Second order convergence of the interface curvature computation in both 2D and 3D.

in order to ensure a robust estimation, we perform an additional quadratic least squares approximation on the curvature field near the interface, similar to [42]. This procedure takes place before the 3D estimation (Eq. (34)), and essentially improves the accuracy of cell-center curvatures by removing possible high-frequency noise. Similarly, the whole procedure is repeated in the y and z directions.

To assess the accuracy of our interface curvature estimation, we calculate the L_∞ norm of a circle/sphere of radius 0.25 centered in a unit square/cube. Table 1 summarizes the error after one step of the calculations on different resolutions, which are also plotted in Fig. 7. Clearly, second-order convergence is achieved in both 2D and 3D cases.

Table 1: Grid convergence of the current interface curvature calculation in both 2D and 3D.

Grid points per diameter		16	32	48	64
L_∞	2D	1.144×10^{-2}	2.904×10^{-3}	1.285×10^{-3}	7.227×10^{-4}
L_∞	3D	1.527×10^{-2}	3.888×10^{-3}	1.732×10^{-3}	9.753×10^{-4}

6. Solution of the Navier-Stokes equations

In this section, we outline the flow solver which is developed from that of Breugem [14] for particle-laden flows. After advancing the level set from ϕ^n to ϕ^{n+1}, the density and viscosity fields are updated by

$$\rho^{n+1} = \rho_1 H_s(\phi^{n+1}) + \rho_2(1 - H_s(\phi^{n+1})), \tag{36a}$$

$$\mu^{n+1} = \mu_1 H_s(\phi^{n+1}) + \mu_2(1 - H_s(\phi^{n+1})), \tag{36b}$$

where

$$H_s(\phi) = \begin{cases} 1 & \text{if} \quad \phi > 0 \\ 0 & \text{otherwise,} \end{cases} \tag{37}$$

is a simple step function.

Next, a prediciton velocity, $\mathbf{u}^*$, is computed by defining $\mathbf{RU}^n$ as

$$\mathbf{RU}^n = -\nabla \cdot (\mathbf{u}^n \mathbf{u}^n) + \frac{1}{Re}\left(\frac{1}{\rho^{n+1}} \nabla \cdot \left[\mu^{n+1}(\nabla \mathbf{u}^n + (\nabla \mathbf{u}^n)^T)\right]\right) + \frac{1}{Fr}\mathbf{g}, \tag{38}$$

which is the right-hand side of the momentum equation (1b) excluding the pressure gradient term. Integrating in time with the second-order Adams-Bashforth scheme yields

$$\frac{\mathbf{u}^* - \mathbf{u}^n}{\Delta t} = \frac{3}{2}\mathbf{RU}^n - \frac{1}{2}\mathbf{RU}^{n-1}. \tag{39}$$

Then, we proceed by solving the Poisson equation for the pressure as in the standard projection method [45], *i.e.*

$$\nabla \cdot \left(\frac{1}{\rho^{n+1}} \nabla p^{n+1}\right) = \frac{1}{\Delta t} \nabla \cdot \mathbf{u}^*. \tag{40}$$

The surface tension between two fluids is also computed during this step, using the ghost fluid method [28] (Sec. 6.2). This allows for an accurate and sharp evaluation of the pressure jump even at large density contrast [30]. Finally, the velocity field at the next time level is updated as

$$\mathbf{u}^{n+1} = \mathbf{u}^* - \frac{\Delta t}{\rho^{n+1}} \nabla p^{n+1}. \tag{41}$$

6.1. Fast pressure-correction method

In the above outline, a Poisson equation of the pressure (Eq. (40)) must be solved at each time step. This operation takes most of the computational time in the projection method, as it is usually solved iteratively. In addition, the operation count of iterative methods depends on the problem parameters (*e.g.* density ratio) and convergence tolerance [13]. On the other hand, Dong and Shen [46] recently developed a velocity-correction method that transforms the variable-coefficient Poisson equation into a constant-coefficient one. The essential idea is to split the pressure gradient term in Eq. (40) in two parts, one with constant coefficients, the other with variable coefficients, *i.e.*

$$\frac{1}{\rho^{n+1}} \nabla p^{n+1} \rightarrow \frac{1}{\rho_0} \nabla p^{n+1} + (\frac{1}{\rho^{n+1}} - \frac{1}{\rho_0}) \nabla \hat{p}, \tag{42}$$

where $\rho_0 = min(\rho_1, \rho_2)$ and $\hat{p}$ is the approximate pressure at time level $n+1$. This splitting reduces to the exact form of Eq. (40) within the lower-density phase, while its validity in the higher-density phase and at the interface depends on the choice of $\hat{p}$. Later, Dodd and Ferrante [13] showed that by explicitly estimating $\hat{p}$ from two previous time levels as

$$\hat{p} = 2p^n - p^{n-1}, \tag{43}$$

the resulting velocity field in Eq. (41) will be second-order accurate in both space and time, for density and viscosity ratios up to 10000. Furthermore, if there are at least two

periodic boundaries (for 3D problems), the constant-coefficient part of Eq. (42) can be solved directly using Gauss elimination in the Fourier domain. Such a FFT-based solver can lead to a speed-up of 10-40 times, thus the name fast pressure-correction method (FastP*). Following this approach, Eqs. (40) and (41) are modified as

$$\nabla^2 p^{n+1} = \nabla \cdot \left[\left(1 - \frac{\rho_0}{\rho^{n+1}}\right) \nabla \hat{p} \right] + \frac{\rho_0}{\Delta t} \nabla \cdot \mathbf{u}^* \tag{44}$$

and

$$\mathbf{u}^{n+1} = \mathbf{u}^* - \Delta t \left[\frac{1}{\rho_0} \nabla p^{n+1} + \left(\frac{1}{\rho^{n+1}} - \frac{1}{\rho_0} \right) \nabla \hat{p} \right]. \tag{45}$$

6.2. Ghost fluid method

As discussed before, surface tension is commonly computed using the continuum surface force (CSF) model [27], in which the pressure jump across an interface is represented as a forcing term on the right-hand side of Eq. (1b). Despite its simplicity, CSF introduces an unfavorable smearing in the density and pressure profiles, resulting in an artificial spreading of the interface (typically over a thickness of $3\Delta x$). An alternative approach is the so-called ghost fluid method (GFM), originally developed by Fedkiw *et al* [28] to capture the boundary conditions in the inviscid compressible Euler equations. Unlike CSF, GFM enables a numerical discretization of the gradient operator while preserving the discontinuity of the differentiated quantity. It was extended to viscous flows by Kang *et al* [**?**] and has been successfully utilized in multiphase flow simulations, see *e.g.* [30, 47, 48].

Recall from Eq. (2) that the pressure jump has two components, one arising from the surface tension, the other from the viscosity difference of the two fluids. In [**?**], a complete algorithm is provided to compute the two contributions, making the density, viscosity, and pressure all sharp. However, having a sharp viscosity profile requires an extra step to evaluate the divergence of the deformation tensor (see Eq. (38)). That is, for cells adjacent to the interface, the second derivatives of the velocity must be evaluated using the techniques developed in [49**?**]. However, rewriting Eq. (2) as

$$[p]_\Gamma = \frac{1}{Re} \left(\frac{1}{Ca} \kappa + 2[\mu]_\Gamma \mathbf{n}^T \cdot \nabla \mathbf{u} \cdot \mathbf{n} \right), \tag{46}$$

reveals that surface tension is the dominant term when the Capillary number, $Ca = We/Re$, is small. For the applications we are interested in, *e.g.* colloidal droplets in microfluidic channels, Ca is of the order of 10^{-5}. Therefore, in the present implementation, we regularize the viscosity profile (*i.e.* replacing $H_s(\phi)$ in Eq. (36b) with $H_\epsilon(\phi)$ in Eq. (18)) and use GFM only for the pressure jump.

6.2.1. Spatial discretization

Eqs. (38), (44), and (45) are discretized on a standard staggered grid using a second-order conservative finite volume method. On a uniform mesh, it is equivalent to central differences in all three directions. A detailed description of the discretization of the individual terms can be found in [13], Sec. 2.2.1. For brevity, we show here only the 2D evaluations of ∇p and $\nabla^2 p$ due to GFM.

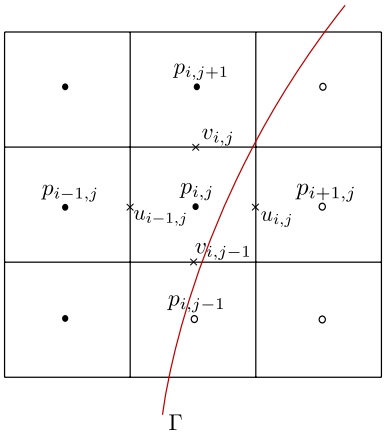

Figure 8: Schematic of the 2D staggered grid where pressure locates at cell centers and velocity components locate at cell faces. The curved line specifies the interface Γ; filled and empty circles indicate discontinuous pressure (or density) values in phase 1 and 2, respectively.

As sketched in Fig. 8, computing $\nabla^2 p$ at node (i, j) requires three entries of p in each direction. If CSF is used, all gradient terms can be evaluated with the straightforward central-difference, *i.e.*

$$(\nabla^2 p)_{i,j} = \frac{p^s_{i-1,j} - 2p^s_{i,j} + p^s_{i+1,j}}{\Delta x^2} + \frac{p^s_{i,j-1} - 2p^s_{i,j} + p^s_{i,j+1}}{\Delta y^2} + O(\Delta x^2). \tag{47}$$

However, the pressure values at the cells adjacent to the interface will have to be smeared out; hence we denote them with p^s. In order for the pressure to be sharp, GFM creates an artificial fluid and assumes that the discontinuity can be extended beyond the physical interface. That is, if we know the corresponding jumps of pressure, then its derivatives can be evaluated using regular finite difference by removing such jumps. For the particular case depicted in Fig. 8, Eq. (47) can be re-written as (see [49] for the intermediate steps)

$$\begin{aligned}(\nabla^2 p)_{i,j} = \frac{p_{i-1,j} - 2p_{i,j} + p_{i+1,j}}{\Delta x^2} - \frac{[p]_{i,j}}{\Delta x^2} - \frac{1}{\Delta x}\left[\frac{\partial p}{\partial x}\right]_{i+1/2,j} \\ + \frac{p_{i,j-1} - 2p_{i,j} + p_{i,j+1}}{\Delta y^2} - \frac{[p]_{i,j-1}}{\Delta y^2},\end{aligned} \tag{48}$$

where we recall $[\cdot]_{i,j}$ denotes the difference between the values in fluid 1 and 2 at cell (i, j) (same for $[\cdot]_{i,j-1}$ *etc*).

To determine the jump terms in Eq. (48), we first note that the velocity and its material derivatives across the interface of viscous flows are continuous, resulting in [**?** 30]

$$\left[\frac{1}{\rho^{n+1}}\nabla p^{n+1}\right]_\Gamma = \mathbf{0}. \tag{49}$$

Furthermore, owing to the splitting that allows us to solve only for a constant-coefficient Poisson equation (Eq. (44)), Eqs. (42) and (49) lead to

$$\left[\frac{1}{\rho_0}\nabla p^{n+1} + (\frac{1}{\rho^{n+1}} - \frac{1}{\rho_0})\nabla \hat{p}\right]_\Gamma = \mathbf{0}. \tag{50}$$

This implies that the pressure term is continuous everywhere (*e.g.* the subscript can be $(i+1/2, j)$).

Then, we discretize the right-hand side of Eq. (44), $RP_{i,j}$, as (except for the pressure-correction term)

$$\begin{aligned} RP_{i,j} = & \left(\big(1 - \frac{\rho_0}{\rho^{n+1}_{i+1/2,j}}\big) \frac{\partial \hat{p}}{\partial x}_{i+1/2,j} - \big(1 - \frac{\rho_0}{\rho^{n+1}_{i-1/2,j}}\big) \frac{\partial \hat{p}}{\partial x}_{i-1/2,j} \right) / \Delta x \\ & + \left(\big(1 - \frac{\rho_0}{\rho^{n+1}_{i,j+1/2}}\big) \frac{\partial \hat{p}}{\partial y}_{i,j+1/2} - \big(1 - \frac{\rho_0}{\rho^{n+1}_{i,j-1/2}}\big) \frac{\partial \hat{p}}{\partial y}_{i,j-1/2} \right) / \Delta y \\ & - \frac{1}{\Delta x} \left[(1 - \frac{\rho_0}{\rho^{n+1}}) \frac{\partial \hat{p}}{\partial x} \right]_{i+1/2,j} + \frac{\rho_0}{\Delta t} \left(\frac{u^*_{i,j} - u^*_{i-1,j}}{\Delta x} + \frac{v^*_{i,j} - v^*_{i,j-1}}{\Delta y} \right), \end{aligned} \tag{51}$$

again using GFM [49]. With a modified right-hand side, $RP^*_{i,j}$, defined as

$$RP^*_{i,j} = RP_{i,j} + \frac{1}{\Delta x} \left[(1 - \frac{\rho_0}{\rho^{n+1}}) \frac{\partial \hat{p}}{\partial x} \right]_{i+1/2,j}, \tag{52}$$

the discretization of Eq. (44) can be written as

$$\frac{p^{n+1}_{i-1,j} - 2p^{n+1}_{i,j} + p^{n+1}_{i+1,j}}{\Delta x^2} + \frac{p^{n+1}_{i,j-1} - 2p^{n+1}_{i,j} + p^{n+1}_{i,j+1}}{\Delta y^2} = \frac{[p]^{n+1}_{i,j}}{\Delta x^2} + \frac{[p]^{n+1}_{i,j-1}}{\Delta y^2} + RP^*_{i,j}, \tag{53}$$

where we have used Eq. (50) to eliminate the jump of the first derivative.

Eq. (53) is still not ready to solve, since the pressure jumps for the first point away from the interface (*e.g.* $[p]^{n+1}_{i,j}$) are not known. Following [30], we perform a Taylor series expansion around Γ,

$$[p]^{n+1}_{i,j} = [p]^{n+1}_{\Gamma} + (x_i - x_\Gamma) \left[\frac{\partial p}{\partial x} \right]^{n+1}_{\Gamma} + O((x_i - x_\Gamma)^2), \tag{54}$$

where $[p]^{n+1}_{\Gamma} = \kappa_\Gamma / We$, and κ_Γ is estimated from Eq. (31) in 2D and from Eq. (34) in 3D, using $\phi^{n+1}_{i,j}$ and $\phi^{n+1}_{i+1,j}$. The jump of the pressure gradient at the interface can be similarly expanded at (i, j)

$$\left[\frac{\partial p}{\partial x} \right]^{n+1}_{\Gamma} = \left[\frac{\partial p}{\partial x} \right]^{n+1}_{i,j} + O(x_\Gamma - x_i), \tag{55}$$

resulting in

$$[p]^{n+1}_{i,j} = \frac{\kappa_\Gamma}{We} + (x_i - x_\Gamma) \left[\frac{\partial p}{\partial x} \right]^{n+1}_{i,j} + O((x_i - x_\Gamma)^2). \tag{56}$$

Using Eq. (50), we can re-write Eq. (56) as

$$[p]^{n+1}_{i,j} = \frac{\kappa_\Gamma}{We} + (x_i - x_\Gamma) \left[(1 - \frac{\rho_0}{\rho^{n+1}}) \frac{\partial \hat{p}}{\partial x} \right]_{i,j} + O((x_i - x_\Gamma)^2), \tag{57}$$

where the jump term on the right-hand side can be explicitly calculated as

$$\left[(1 - \frac{\rho_0}{\rho^{n+1}}) \frac{\partial \hat{p}}{\partial x} \right]_{i,j} = \left[1 - \frac{\rho_0}{\rho^{n+1}} \right]_{i,j} \frac{\partial \hat{p}}{\partial x}_{i,j} + \left(1 - \frac{\rho_0}{\rho^{n+1}_{i,j}} \right) \left[\frac{\partial \hat{p}}{\partial x} \right]_{i,j}, \tag{58}$$

using the reduced identity of $[AB]_{i,j} = [A]_{i,j}B + A[B]_{i,j}$ [**?**]. Eqs. (57) and (58) thus provide a second-order estimation of $[p]_{i,j}^{n+1}$ in Eq. (53) (similarly for $[p]_{i,j-1}^{n+1}$).

We can also keep only the leading-order term, *i.e.*

$$[p]_{i,j}^{n+1} = \frac{\kappa_\Gamma}{We} + O(x_i - x_\Gamma). \tag{59}$$

This way, the pressure jump varies simply with the interface curvature, and it is second-order accurate when the density is uniform. For the test cases shown below, Eq. (59) is used. Thus, we can re-write Eq. (53) as

$$\frac{p_{i-1,j}^{n+1} - 2p_{i,j}^{n+1} + p_{i+1,j}^{n+1}}{\Delta x^2} + \frac{p_{i,j-1}^{n+1} - 2p_{i,j}^{n+1} + p_{i,j+1}^{n+1}}{\Delta y^2} = \frac{\kappa_\Gamma}{We}\left(\frac{1}{\Delta x^2} + \frac{1}{\Delta y^2}\right) + RP_{i,j}^*, \tag{60}$$

Clearly, the resulting linear system has a standard symmetric coefficient matrix, and it can be solved directly using the FFT-based Poisson solver (Sec. 6.1). Care should be exercised when a nodal point cross the interface in more than one direction. In those cases, we average the interface curvature of each crossing direction to avoid numerical oscillations. Additionally, when taking the gradient of the pressure-correction term; *e.g.* its derivative along the x direction, the correct discretization should be

$$\frac{\partial \hat{p}}{\partial x}_{i,j} = \frac{\left(\hat{p}_{i+1,j} - (2[p]_{i+1,j}^{n} - [p]_{i+1,j}^{n-1})\right) - \hat{p}_{i,j}}{\Delta x}. \tag{61}$$

After removing the jump, the divergence of the bracket term is evaluated in the same way as in [13].

Finally, we can re-write Eqs. (44) and (45) compactly as

$$\nabla^2 p^{n+1} = \nabla_g^2 [p]_\Gamma + \nabla \cdot \left[\left(1 - \frac{\rho_0}{\rho^{n+1}}\right)\nabla_g \hat{p}\right] + \frac{\rho_0}{\Delta t}\nabla \cdot \mathbf{u}^*, \tag{62}$$

$$\mathbf{u}^{n+1} = \mathbf{u}^* - \Delta t\left[\frac{1}{\rho_0}\nabla_g p^{n+1} + \left(\frac{1}{\rho^{n+1}} - \frac{1}{\rho_0}\right)\nabla_g \hat{p}\right]. \tag{63}$$

where ∇_g and ∇_g^2 denote, respectively, the gradient operator considering the jump and the extra jump terms from the laplacian operator due to GFM.

6.3. Time integration

In the current work, a second-order accurate Adams-Bashforth scheme is used for the time integration. The time step is restricted by convection, diffusion, surface tension, and gravity, due to our explicit treatment of these terms. As suggested in [**?**], the overall time step restriction is

$$\Delta t \leqslant 1 \Big/ \left(C_{CFL} + V_{CFL} + \sqrt{(C_{CFL} + V_{CFL})^2 + 4G_{CFL}^2 + 4S_{CFL}^2}\right), \tag{64}$$

where C_{CFL}, V_{CFL}, G_{CFL}, and S_{CFL} are the "speeds" due to convection, viscosity, gravity, and surface tension, respectively. Specifically, they are given as

$$C_{CFL} = \frac{|u|_{max}}{\Delta x} + \frac{|v|_{max}}{\Delta y} + \frac{|w|_{max}}{\Delta z}, \tag{65}$$

$$V_{CFL} = \frac{1}{Re} max\left(\frac{\mu_1}{\rho_1}, \frac{\mu_2}{\rho_2}\right)\left(\frac{2}{\Delta x^2} + \frac{2}{\Delta y^2} + \frac{2}{\Delta z^2}\right), \tag{66}$$

$$G_{CFL} = \sqrt{\frac{1}{Fr}\frac{|(1 - \frac{\rho_1+\rho_2}{2\rho})g|_{max}}{min(\Delta x, \Delta y, \Delta z)}}, \tag{67}$$

$$S_{CFL} = \sqrt{\frac{\sigma|\kappa|_{max}}{min(\rho_1, \rho_2)\big[min(\Delta x, \Delta y \Delta z)\big]^2}}. \tag{68}$$

where $|\kappa|_{max}$ in (68) can be approximated by $1/\Delta x$ in 2D and $2/\Delta x$ in 3D, assuming Δx is the smallest grid spacing.

The reasons we choose an explicit temporal scheme rather than an implicit one are twofold. First, for applications involving a large density and viscosity contrast, the stability restriction imposed by surface tension is usually greater than that imposed by diffusion. Second, an implicit formulation of GFM has been admitted to be challenging to develop [30], and it was shown in a recent study [50] that a capillary time-step constraint exists, irrespective of the type of implementation, due to the temporal sampling of surface capillary waves. Fortunately, the fast pressure-correction method enables the use of FFT for the constant-coefficient Poisson equation and hence an accurate and fast solution of the two-fluid Navier-Stokes equation can be obtained.

6.4. Full solution procedure

We summarize the full solution procedure as follows:

1. Advance the interface explicitly from ϕ^n to ϕ^{n+1} using the iCLS, and update the density ρ^{n+1} and the viscosity μ^{n+1}.

2. Advance the velocity field explicitly from $\mathbf{u}^n$ to $\mathbf{u}^*$ with Eqs. (38) and (39).

3. Project the velocity field by solving the constant-coefficient Poisson Eq. (62) making use of the FastP* and the GFM.

4. Update the velocity from $\mathbf{u}^*$ to $\mathbf{u}^{n+1}$ explicitly with Eq. (63), again using the FastP* and the GFM.

6.5. Validations

6.5.1. Spurious currents

A common problem in mulitiphase-flow simulations is the artificial velocity generated at the fluid interface due to errors in the curvature computation. To access the significance of such spurious currents, we test a stationary droplet of diameter $D = 0.4$ placed at the center of a unit box. The surface tension between the inner and outer fluid is $\sigma = 1$, the viscosity is uniformly $\mu = 0.1$, and the density ratio is 1. By changing the density ρ of both fluids, the Laplace number $La = \sigma\rho D/\mu^2$ can be varied. The spurious currents are thus determined from the resulting capillary number $Ca = |U_{max}|\mu/\sigma$ at a non-dimensional time $t\sigma/(\mu D) = 250$. Here, we compare the results on a 32×32 mesh with the GFM implementation by Desjardins *et al* [30]. As listed in Table 2, the capillary numbers from both tests remain very small for all the Laplace numbers, with the present results being one-order smaller.

Table 2: Dependence of spurious current capillary number Ca on the Laplace number for a static droplet with surface tension on a 32×32 mesh in comparison with Desjardins *et al* [30].

La	12	120	1,200	12,000	120,000	1,200,000
Ca	2.85×10^{-6}	3.14×10^{-6}	3.63×10^{-6}	3.87×10^{-6}	3.41×10^{-6}	5.79×10^{-7}
Ca from [30]	4.54×10^{-5}	3.67×10^{-5}	3.62×10^{-5}	4.15×10^{-5}	3.75×10^{-5}	8.19×10^{-6}

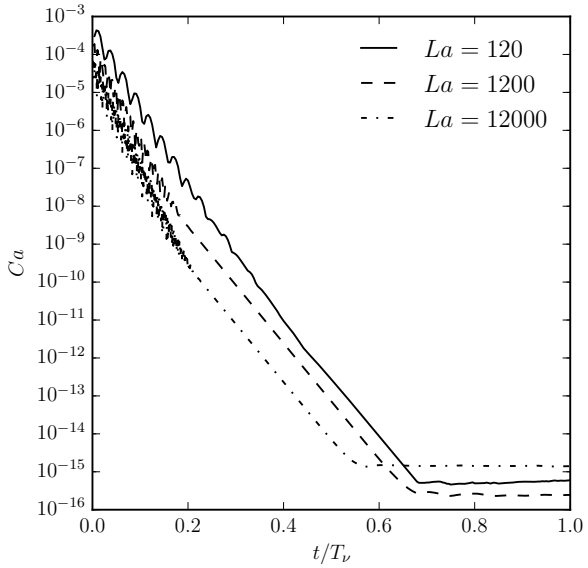

Figure 9: Temporal evolution of the spurious currents without performing level set reinitialization at three Laplace numbers as in [51].

We also note that the spurious currents reported in Table 2 are obtained by performing the level set reinitialization at about every 100 time steps. However, if we turn off the reinitialization, such spurious velocity will eventually go to machine zero, as shown in Fig. 9, where time is non-dimensionalized with the viscous time scale, $T_\nu = \rho D^2/\mu$. The nearly exponential decay of Ca and the collapsing of the three curves are the result of the viscous damping of the spurious velocity, as the shape of droplet relaxes to its numerical equilibrium. Similar results are obtained and explained in greater detail in [51] using a balanced-force continuum-surface-force surface-tension formulation and the VOF. The result in Fig. 9 therefore validates the computation of the surface tension with the GFM.

6.5.2. Capillary wave

To verify our solver at large density and (dynamic) viscosity contrasts, we simulate a small-amplitude capillary wave for which there exists an analytical solution derived by Prosperetti [52]. Specifically, this case involves two immiscible, viscous fluids separated by an interface initialised with a sinusoidal shape. When gravity is neglected, the balance between inertia, viscosity, and surface tension results in a decaying free-surface wave. By requiring matching kinematic viscosity $\nu_1 = \nu_2$, the evolution of the wave amplitude can be derived analytically and compared with the simulation results.

We set up our simulation in the same way as suggested in [13]. Here, two fluids of

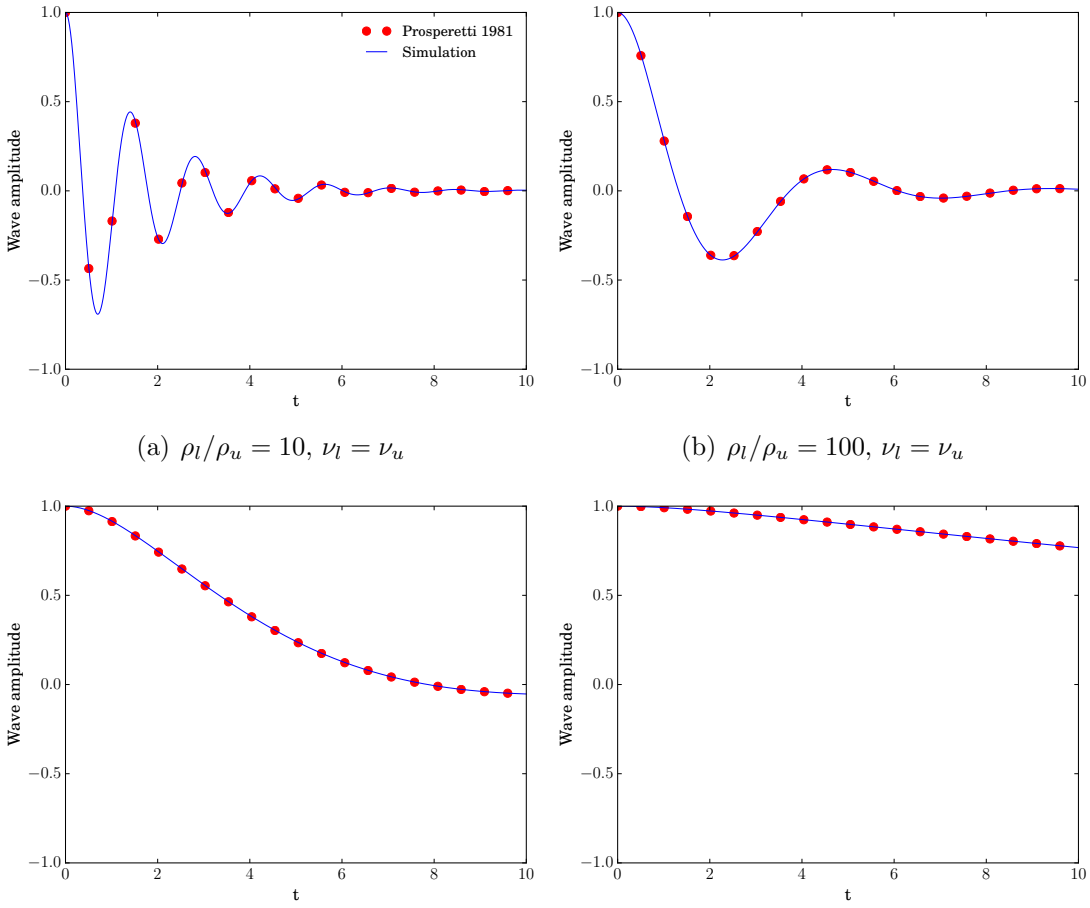

(a) $\rho_l/\rho_u = 10$, $\nu_l = \nu_u$ (b) $\rho_l/\rho_u = 100$, $\nu_l = \nu_u$

(c) $\rho_l/\rho_u = 1000$, $\nu_l = \nu_u$ (d) $\rho_l/\rho_u = 10000$, $\nu_l = \nu_u$

Figure 10: Time development of the capillary wave amplitude (normalized to a_0) for increasing density ratios and matching kinematic viscosity in comparison with Prosperetti's analytical solution [52].

equal depth are placed in a 1×3 (64×192 grid points) domain, where the streamwise direction ($L = 1$) is periodic and the vertical direction ($H = 3$) wall-bounded. The interface has an initial wavelength of $\lambda = 1$ and an amplitude of $a_0 = 0.01$. With varying density ratios ρ_2/ρ_1, the non-dimensional parameters for the test are

$$Re = 100, \quad We = 1, \quad Fr = \infty, \quad \rho_2/\rho_1 = 10 - 10,000, \quad \nu_1 = \nu_2. \tag{69}$$

The CFL number, $\Delta t/\Delta x$, is 2.5×10^{-2} for $\rho_2/\rho_1 = 10$ and 10^2, and it is reduced to 2.5×10^{-3} for $\rho_2/\rho_1 = 10^3$ and 2.5×10^{-4} for $\rho_2/\rho_1 = 10^4$.

Fig. 10 shows the temporal evolution of the wave amplitude up to $t = 10$. The excellent agreement with Prosperetti's analytical solution [52] confirms the normal stress balance computed using the GFM and the FastP*. Note that the dynamic viscosity ratio, μ_2/μ_1, also varies from 10 to 10000. However, neglecting its contribution to the pressure jump by regularizing the viscosity profile yields accurate results since the Capillary number is small ($Ca = We/Re = 0.01$), as discussed in conjunction with Eq. (46).

6.5.3. Rising bubble

Finally, we compute four cases of a rising bubble to access the overall accuracy of the current iCLS-NS solver in 3D in the presence of moderate deformations. Originally documented by Grace [53], it is observed that a single gas bubble rising in quiescent liquid has four characteristic shapes: spherical, ellipsoidal, skirted, or dimpled. The governing non-dimensional numbers are the Morton number M, Eotvos number Eo, and the terminal Reynolds number Re_t, defined as

$$M = \frac{g\mu_l^4}{\rho_l \sigma^3}, \quad Eo = \frac{\Delta\rho g d^2}{\sigma}, \quad Re_t = \frac{\rho_l U_\infty d}{\mu_l}, \tag{70}$$

where d is the bubble diameter, $\Delta\rho$ is the density difference, U_∞ is the terminal velocity of the bubble, and the subscripts l and g denote, in order, the liquid and gas phase. The Morton and Eotvos number are defined purely by the material properties of the chosen fluids, while the terminal Reynolds number provides a measure of the steady-state bubble velocity.

Table 3 lists the four representative cases we select for the simulations. A spherical bubble of diameter $d = 1$ is centered in a domain of size $(L_x \times L_y \times L_z) = (3d \times 6d \times 3d)$. A grid of $96 \times 192 \times 96$ points is used, giving the bubble an initial resolution of 32 points per diameter. Periodic boundary conditions are imposed in the x (spanwise) and y (rising) directions whereas no friction, no penetration is enforced in the z direction. As suggested by Annaland *et al* [54], a ratio of 100 between the density and viscosity of liquid and gas is sufficiently high to approximate such gas-liquid systems, leading to $\Delta\rho \approx \rho_l$. Re and We in Eq. (3) can thus be obtained from M and Eo as

$$Re = \left(\frac{Eo^3}{M}\right)^{1/4}, \quad We = Eo. \tag{71}$$

The CFL number, $\Delta t/\Delta x$, is 1.6×10^{-4} for cases (a), (b), and (d), and 1.6×10^{-3} for case (c). The simulation is integrated in time up to $t = 10$ to ensure the bubble reaches nearly steady state.

The results of the bubble terminal velocities are presented in Table 3. The difference between the computed Reynolds, Re_C, and the terminal Reynolds, Re_G, measured by Grace [53] remains small for all four cases. The bubble mass is conserved, with a maximal mass loss of about 0.02% found in the skirted case, where the bubble undergoes a large and rapid deformation. The corresponding bubble shapes are illustrated in Fig. 11, which clearly displays spherical, ellipsoidal, skirted, and dimpled shapes. We can therefore conclude that the dynamics of a single rising bubble is well-captured.

7. Droplet interactions

7.1. Extension to multiple level sets

The present level set approach can be readily applied to modeling of a single droplet or a number of droplets, thanks to its Eulerian nature. Since a single marker function is used, we call it single level set (SLS) method. SLS can also be extended to multiple level sets (MLS), so that each droplet has its own color function. This has several benefits including distinction and tracking of each droplet, independent curvature computation, and ability to prevent numerical coalescence [47], *etc.* Although the computational cost

Table 3: Comparison of computed terminal Reynolds number (Re_C) and experimental terminal Reynolds number (Re_G) obtained from the Grace diagram [53] under four different Morton (M) and Eotvos (Eo) numbers.

Case	Bubble regime	M	Eo	Re_G	Re_C	Mass loss (%)
(a)	Spherical	1×10^{-3}	1	1.7	1.73	9.86×10^{-5}
(b)	Ellipsoidal	0.1	10	4.6	4.57	3.32×10^{-4}
(c)	Skirted	1	100	20	19.21	1.64×10^{-2}
(d)	Dimpled	1000	100	1.5	1.71	3.28×10^{-3}

(a) Spherical (b) Ellipsoidal (c) Skirted (d) Dimpled

Figure 11: Bubble shapes resulting from different Morton (M) and Eotvos (Eo) numbers, as indicated in Table 3.

may increase with the number of the level set functions, with the narrow band approach [39], the overall cost is comparable to using SLS.

The extension from SLS to MLS is straightforward. Assuming no droplets will overlap, each level set function is simply advected successively. When two droplets get close, however, a minor modification of the GFM is required to account for the additional pressure jump from a neighbouring droplet. As sketched in Fig. 12, when two interfaces are within two grid cells, pressure jump across each interface needs to be considered and superimposed. That is, Eq. (48) (corresponding to Fig. 8) should be modified as

$$\begin{aligned}(\nabla^2 p)_{i,j} = \frac{p_{i-1,j} - 2p_{i,j} + p_{i+1,j}}{\Delta x^2} - 2\frac{[p]_{i,j}}{\Delta x^2} - \frac{1}{\Delta x}\left[\frac{\partial p}{\partial x}\right]_{i+1/2,j} + \frac{1}{\Delta x}\left[\frac{\partial p}{\partial x}\right]_{i-1/2,j} \\ + \frac{p_{i,j-1} - 2p_{i,j} + p_{i,j+1}}{\Delta y^2} - \frac{[p]_{i,j-1}}{\Delta y^2},\end{aligned} \tag{72}$$

Similarly, all the jumps should be removed when computing the pressure gradient. The formulas (Eqs. (62) and (63)) remain the same as in SLS.

7.2. Near-field interactions

Apart from the hydrodynamic interactions arising from the Navier-Stokes equations, colloidal droplets transported in microfluidic devices are often subject to other forms of interactions, such as the depletion potential due to the presence of surfactant micelles. The depletion potential can induce a near-field attracting force [55, 5], and it plays a key role in the droplet dynamics [7]. Below, we first provide a brief background on the theory of depletion potential, then present a numerical method to enforce the depletion potential based on MLS and GFM.

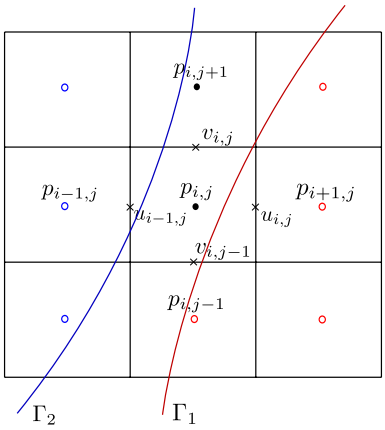

Figure 12: Pressure jump in the presence of multiple interfaces within two grid cells. Red and blue circles indicate nodal pressure in droplet 1 and 2, respectively. (For interpretation of the references to color in this figure legend, the reader is referred to the web version of this article.)

7.2.1. Theory of depletion potential

The original model of depletion potential proposed by Asakura and Oosawa [55] assumes the surfactant micelles as rigid spheres. As illustrated in Fig. 13, a suspension of such small spheres around the larger colloidal/non-colloidal droplets creates an osmotic pressure on the droplet surface. When the distance between two droplets is less than the diameter of the surfactant micelles, there will be a pressure defect due to the exclusion of the surfactants. This is the mechanism for the attracting depletion force. Alternatively, the same conclusion can be deduced from a thermodynamic point of view. That is, an increase of the volume accessible to the small spheres will increase the total entropy of the system, so that the larger sphere will tend to get closer to exclude the smaller ones [56]. The second argument justifies the depletion force even when the droplets are deformable. Furthermore, it gives the following expression for the depletion potential, $U(r)$, for two large, rigid spheres separated by a distance r,

$$U(r) = \begin{cases} \infty & \text{if} \quad r \leqslant 2R \\ p_{os} V_{ex} & \text{if} \quad 2R < r \leqslant 2R + 2r_s \\ 0 & \text{otherwise,} \end{cases} \tag{73}$$

where V_{ex} is the excluded volume and p_{os} is the osmotic pressure. In order, they are given as

$$V_{ex} = \frac{4\pi(R + r_s)^3}{3}\left[1 - \frac{3r}{4(R + r_s)} + \frac{r^3}{16(R + r_s)^3}\right]. \tag{74}$$

and

$$p_{os} = -kTN/V, \tag{75}$$

where k is the Boltzmann constant, T is temperature, N is the number of small spheres, V is the total volume of the solution. Note that the negative value of p_{os} corresponds to attraction between droplets.

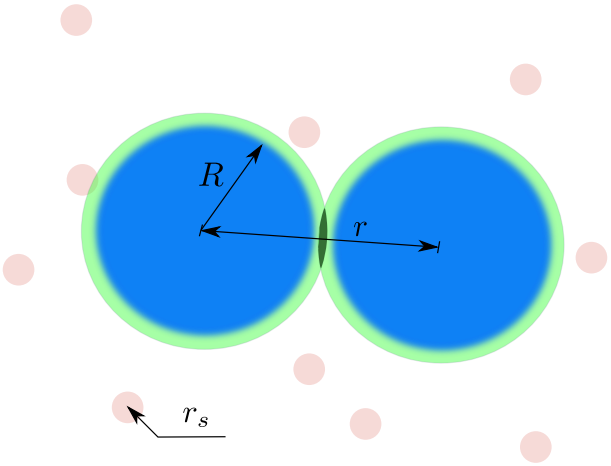

Figure 13: Depletion of surfactant micelles of radius r_s between larger colloidal particles of radius R, separated by distance r. The green shells around larger spheres represent volume from which the centers of small spheres are excluded. The dark region shows the overlap volume. (For interpretation of the references to color in this figure legend, the reader is referred to the web version of this article.)

7.2.2. MLS/GFM-based method for computing the depletion potential

Before linking the preceding depletion potential with a Navier-Stokes solver, we comment on two observations. First, the origin of the depletion force as an imbalance of osmotic pressure implies a resemblance with surface tension, which causes the pressure to jump across the interface to minimize interfacial energy. This hints that similar methods, *e.g.* CSF or GFM, can be used to model such potential. Second, a level set contest seems convenient to represent the dependence of the depletion potential on the distance. In fact, the identification of the overlap region is straightforward with MLS. Therefore, we propose an algorithm as laid out in Algorithm 1.

The overall idea of Algorithm 1 is to consider the depletion potential in the projection step through the use of MLS and GFM. Specifically, the osmotic pressure p_{os} manifests itself as a modification term on the right-hand side of Eq. (62), and it is a pressure drop when entering the overlap region, which has to be removed when exiting [2]. The value of this pressure defect, $\nabla_g^2 p_{os}$, is evaluated in the same way as in GFM. To find all the possible interacting pairs among N droplets, two loops of at least $N!(N-2)!/2$ counts are executed. Eventually, equations (62) and (63) are modified as

$$\nabla^2 p^{n+1} = \nabla_g^2([p] - p_{os}) + \nabla \cdot \left[\left(1 - \frac{\rho_0}{\rho^{n+1/2}}\right) \nabla_g \hat{p} \right] + \frac{\rho_0}{\Delta t} \nabla \cdot \mathbf{u}^*, \tag{76}$$

and

$$\mathbf{u}^{n+1} = \mathbf{u}^* - \Delta t \left[\frac{1}{\rho_0} \nabla_g p^{n+1} + \left(\frac{1}{\rho^{n+1/2}} - \frac{1}{\rho_0} \right) \nabla_g \hat{p} \right]. \tag{77}$$

[2] In Alg. 1, $\nabla_g^2 p_{os}$ is subtracted from $RP_{i,j,k}$ for pressure drop because it is added on the left-hand side. Same for the next line when it is removed.

Algorithm 1: A pseudo code for computation of depletion potential.

```
Enter the pressure solver. Compute the right-hand side of (62), RP_{i,j,k}, without
the osmotic pressure;
Compute p_os from (75) (a constant);
for m = 1 : (N − 1) do
    Get φ_m    ! level set for droplet m
    for n = (m + 1) : N do
        Get φ_n    ! level set for droplet n
        where φ_m < r_s and φ_n < r_s do tag as overlap
        forall the i, j, k do
            if overlap then
                RP_{i,j,k} = RP_{i,j,k} − ∇²_g p_os    ! add pressure drop entering the overlap
                region
            else
                RP_{i,j,k} = RP_{i,j,k} + ∇²_g p_os    ! remove pressure drop exiting the outer
                region
            end
        end
    end
end
Solve for p^{n+1} from Eq. (76) using the FastP* and GFM. Exit the pressure solver.
```

7.2.3. Discussion on the MLS/GFM-based method

In this section, we elaborate on the idea of the MLS/GFM-based method for the computation of the depletion potential. In the original model, the depletion potential is calculated based on hard spheres (Eq. (74)). Although it also applies to deformable droplets, it is not very straightforward to derive the potential as a function of distance in general. With the aid of MLS, nevertheless, looking for overlap regions become convenient. In essence, the difficulty of calculating an arbitrary volume has been replaced with identifying the overlap of two iso-contours, which is embedded naturally in the level set function. Note also that, the depletion potential can be computed not just between two droplets, but can also be between a droplet and a wall, *etc.*

In terms of the pressure defect in the gap between two droplets, GFM ensures that a sharp jump is maintained without numerical spreading while a divergence-free velocity field is obtained after the correction. The same spatial discretization (central difference) and temporal scheme (Adam-Bashforth) are applied to this pressure jump, leading to second order accuracy in both space and time. One remaining question is how to avoid overlap between the droplets. Following Eq. (74) the potential would go to infinity at contact. Numerically, we simply turn off the depletion potential when the minimal distance between two droplets are less than the grid resolution, Δx. As will be shown next, it practically prevents overlapping.

Approaching drops. We verify our method by simulating two or three equal-sized droplets in a quiescent fluid environment and observe how they approach each other due to depletion potential. Specifically, we set the droplet diameter $d = 1$, the computational domain $3 \times 3 \times 3$, and a resolution of $\Delta x = 1/32$. The viscosity and density ratios of the

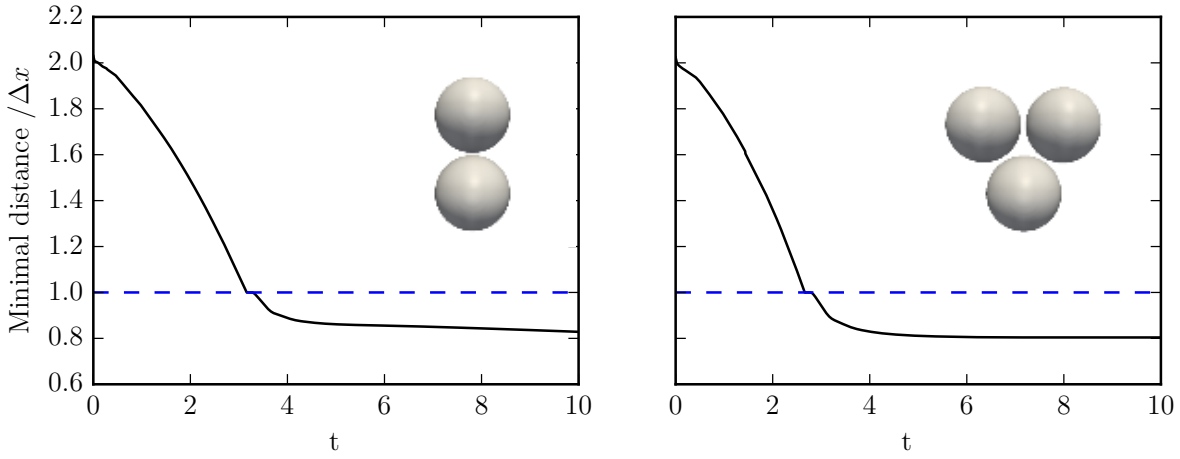

(a) Two droplets

(a) Three droplets

Figure 14: Minimal distance between the droplet surfaces as function of time in the presence of depletion forces. Simulation of (a) two droplets and (b) three droplets suspended in an initially quiescent fluid. Due to symmetry, only the minimal distance is plotted.

droplet to the ambient fluid are 1.4 and 1.8, respectively, corresponding to a fluorinated oil droplet in water. The non-dimensional parameters are chosen as $Re = 10$, $We = 0.1$, and $Fr = \infty$, leading to a Capillary number of 0.01 and neglected gravity. The pressure defect is set to be $p_{os} = -40$.

The results of these tests are shown in Fig. 14 up to $t = 10$. The droplets, originally separated by a distance of $2\Delta x$, gradually get closer, to a distance lower than the grid spacing Δx. At Δx, a short plateau appears in the distance profile, which is expected since the depletion potential is suddenly cut off. The overall smooth approach validataes our method of the MLS/GFM-based depletion potential.

8. Conclusion

A numerical method mainly intended for the hydrodynamic simulations of colloidal droplets in microfluidic devices has been developed and validated. The code is based on a fast, second-order-accurate solver of the incompressible, two-fluid Navier-Stokes equations, and uses a mass-conserving level set method to capture the fluid interface. This combination provides a general framework for any multiphase flow problems (see e.g. our recent study on jet instabilities [57]), and allows us to develop specific methods for the simulations of droplets in saturated surfactant suspensions with depletion forces as in the recent experiment in [7]. Particularly, we have developed or extended four numerical techniques to improve the general accuracy:

1. A mass-conserving, interface-correction level set method (iCLS) is proposed. As a standalone level set module, it is efficient, accurate, guarantees global mass conservation, and is simple to implement. It also enables corrections that can depend on the local curvature or any other parameter of interest.

2. A simple estimation of the interface curvature based on nodal curvature is introduced. As an important ingredient both for the mass correction (iCLS) and the surface tension computation, we show that our estimation converges in second-order both in 2D and 3D, and can lead to machine-zero spurious currents for a stationary 2D droplet.

3. The ghost fluid method (GFM) for the computation of surface tension is combined with the FastP* method [13]. This enables the use of FFT for the direct pressure solver, and can accurately account for surface tension at large density ratios.

4. A ghost fluid/multiple level set (GFM/MLS-based) method is also proposed to compute the pressure defect caused by a depletion potential between multiple droplets or between droplets and a nearby wall. The approach can possibly be extended to account for surfactant diffusion at the interface and in the liquid.

The last technique applies specifically to the simulation of colloidal droplets in microfluidic devices. This will enable us to further explore the effects of the near-field interactions as those observed experimentally in [7], and potentially improve the design of microfluidic devices. In addition, the combination of the GFM for sharp interfaces and the FastP* method [13] can be exploited for the simulations of droplet in turbulent flows as in [58], adding an accurate representation of evaporation thanks to the iCLS approach proposed here.

Acknowledgements

The work is supported by the Microflusa project. This effort receives funding from the European Union Horizon 2020 research and innovation programme under Grant Agreement No. 664823. O.T. acknowledges support from Swedish Research Council (VR) through the Grant Nr. 2013-5789. L.B. and J.-C.L. also acknowledge financial support by the European Research Council grant, no. ERC-2013-CoG-616186, TRITOS. The computer time was provided by SNIC (Swedish National Infrastructure for Computing). Last but not least, Z.G. thanks Mehdi Niazi, Michael Dodd, Walter Fornari, Dr. Olivier Desjardins, Dr. Marcus Herrmann, and Dr. David Salac for interesting and helpful discussions.

References

[1] Y. Xia, B. Gates, Y. Yin, and Y. Lu. Monodispersed colloidal spheres: old materials with new applications. *Adv. Mater.*, 12:693–713, 2000.

[2] O.D. Velev and S. Gupta. Materials fabricated by micro- and nanoparticle assembly - the challenging path from science to engineering. *Adv. Mater.*, 21:1897–1905, 2009.

[3] F. Li, D.P. Josephson, and A. Stein. Colloidal assembly: the road from particles to colloidal molecules and crystals. *Angew. Chem. Int. Ed.*, 50:360–388, 2011.

[4] S. Sacanna and D.J. Pine. Shape-anisotropic colloids: building blocks for complex assemblies. *Curr. Opin. Colloid Interface Sci.*, 16:96–105, 2011.

[5] J. Mewis and N.J. Wagner. *Colloidal suspension rheology.* Cambridge University Press, New York, USA, 2012.

[6] Gi-Ra Yi, D.J. Pine, and S. Sacanna. Recent progress on patchy colloids and their self-assembly. *J. Phys.: Condens. Matter*, 25:193101, 2013.

[7] B. Shen, J. Ricourvier, F. Malloggi, and P. Tabeling. Designing colloidal molecules with microfluidics. *Adv. Sci.*, 1600012:1–7, 2016.

[8] C. Pozrikidis. *Boundary integral and singularity methods for linearized viscous flow.* Cambridge University Press, New York, USA, 1992.
[9] A. Kumar and M.D. Graham. Accelerated boundary integral method for multiphase flow in non-periodic geometries. *J. of Comput. Phys.*, 231:6682–6713, 2012.
[10] L. Zhu, C. Rorai, M. Dhrubaditya, and L. Brandt. A microfluidic device to sort capsules by deformability: a numerical study. *Soft Matt.*, 10:7705–7711, 2014.
[11] M. Wörner. Numerical modeling of multiphase flows in microfluidics and micro process engineering: a review of methods and applications. *Microfluid Nanofluid*, 12:841–886, 2012.
[12] C. Galusinski and P. Vigneaus. On stability condition for bifluid flows with surface tension: Application to microfluidics. *J. of Comput. Phys.*, 227:6140–6164, 2008.
[13] M.S. Dodd and A. Ferrante. A fast pressure-correction method for incompressible two-fluid flows. *J. of Comput. Phys.*, 273:416–434, 2014.
[14] W.-P. Breugem. Numerical simulation of drop impact on a liquid-liquid interface with a multiple marker front-capturing method. *J. of Comput. Phys.*, 228:4444–4467, 2012.
[15] R. Scardovelli and S. Zaleski. Direct numerical simulation of free-surface and interfacial flow. *Ann. Rev. Fluid Mech.*, 31:567–603, 1999.
[16] J.A. Sethian. *Level set method and fast marching method.* Cambridge University Press, New York, USA, 1999.
[17] M. Sussman, P. Smereka, and S. Osher. A level set approach for computing solutions to incompressible two-phase flow. *J. of Comput. Phys.*, 114:146–159, 1994.
[18] R.R. Nourgaliev and T.G. Theofanous. High-fidelity interface tracking in compressible flows: unlimited anchored adaptive level set. *J. of Comput. Phys.*, 227:836–866, 2007.
[19] M. Sussman and E. Fatemi. An efficient, interface-preserving level set redistancing algorithm and its application to interfacial incompressible fluid flow. *J. Sci. Comput.*, 20:1165–1191, 1997.
[20] M. Herrmann. A balanced force refined level set grid method for two-phase flows on unstructured flow solver grids. *J. of Comput. Phys.*, 227:2674–2706, 2008.
[21] M. Sussman and E.G. Puckett. A coupled level set and volume-of-fluid method for computing 3d and axisymmetric incompressible two-phase flows. *J. of Comput. Phys.*, 162:301–337, 2000.
[22] S.P. van der Pijl, A. Segal, C. Vuik, and P. Wesseling. Computing three-dimensional two-phase flows with a mass-conserving level set method. *Comput. Vis. Sci.*, 11:221–235, 2008.
[23] K. Luo, C. Shao, Y. Yang, and J. Fan. An mass conserving level set method for detailed numerical simulation of liquid atomization. *J. of Comput. Phys.*, 298:495–519, 2015.
[24] E. Olsson and G. Kreiss. A conservative level set method for two phase flow. *J. Comput. Phys.*, 210:225–246, 2005.
[25] V. Sabelnikov, A. Yu. Ovsyannikov, and M. Gorokhovski. Modified level set equation and its numerical assessment. *J. of Comput. Phys.*, 278:1–30, 2014.
[26] D. Salac. A general, mass-preserving navier-stokes projection method. *Comput. Phys. Comm.*, 204:97–106, 2016.
[27] J. Brackbill, D. Kothe, and C. Zemach. A continuum method for modeling surface tension. *J. of Comput. Phys.*, 100:335–354, 1992.
[28] R.P. Fedkiw, T. Aslam, B. Merriman, and S. Osher. A non-oscillatory eulerian approach to interfaces in multimaterial flows (the ghost fluid method). *J. of Comput. Phys.*, 152:457–492, 1999.
[29] M. Kang, R.P. Fedkiw, and X.-D. Liu. A boundary condition capturing method for multiphase incompressible flow. *J. Sci. Comput.*, 15:323–360, 2000.
[30] O. Desjardins, V. Moureau, and H. Pitsch. An accurate conservative level set/ghost fluid method for simulating turbulent atomization. *J. of Comput. Phys.*, 227:8395–8416, 2008.
[31] X.-D. Liu, S. Osher, and T. Chan. Weighted essentially non-oscillatory schemes. *J. of Comput. Phys.*, 115:200–213, 1994.
[32] W. Mulder, S. Osher, and J.A. Sethian. Computing interface motion in compressible gas dynamcis. *J. of Comput. Phys.*, 100:209–228, 1992.
[33] O. Desjardins and H. Pitsch. A spectrally refined interface approach for simulating multiphase flows. *J. of Comput. Phys.*, 228:1658–1677, 2009.
[34] G. Velmurugana, Kolahdouzb E.M., and D. Salac. Level set jet schemes for stiff advection equations: The semijet method. *ArXive*, 1509.0283, 2016.
[35] C.-W. Shu and S. Osher. Efficient implementation of essentially non-oscillatory shock-capturing schemes. *J. of Comput. Phys.*, 77:439–471, 1988.

[36] S.T. Zalesak. Fully multidimensional flux-corrected transport algorithms for fluids. *J. of Comput. Phys.*, 31:335–362, 1979.
[37] G. Russo and P. Smereka. A remark on computing distance functions. *J. of Comput. Phys.*, 163:51–67, 2000.
[38] M. Owkes and O. Desjardins. A discontinuous galerkin conservative level set scheme for interface capturing in multiphase flows. *J. of Comput. Phys.*, 249:275–302, 2013.
[39] D. Adalsteinsson and J.A. Sethian. A fast level set method for propagating interfaces. *J. of Comput. Phys.*, 111(2):269–277, 1995.
[40] D. Peng, B. Merriman, S. Osher, H. Zhao, and M. Kang. A pde-based fast local level set method. *J. of Comput. Phys.*, 155:410–438, 1999.
[41] B. Engquist, A.-K. Tornberg, and R. Tsai. Discretization of dirac delta functions in level set methods. *J. Comput. Phys.*, 207:28–51, 2005.
[42] E. Marchandise, P. Geuzaine, N. Chevaugeon, and J.-F. Remacle. A stabilized finite element method using a discontinuous level set approach for the computation of bubble dynamics. *J. of Comput. Phys.*, 225:949–974, 2007.
[43] M.M. Francois, S.J. Cummins, E.D. Dendy, D.B. Kothe, J.M. Sicilian, and M.W. Williams. A balanced force algorithm for continuous and sharp interfacial surface tension models within a volume tracking framework. *J. of Comput. Phys.*, 213:141–173, 2006.
[44] J. Luo, X.Y. Hu, and N.A. Adams. A conservative sharp interface method for incompressible multiphase flows. *J. of Comput. Phys.*, 284:547–565, 2015.
[45] A.J. Chorin. Numerical solution of the navier-stokes equations. *Math. Comput.*, 22:745–762, 1968.
[46] S. Dong and J. Shen. A time-stepping scheme involving constant coefficient matrices for phase-field incompressible flows with large density ratios. *J. of Comput. Phys.*, 231:5788–5804, 2012.
[47] E. Coyajee and B.J. Boersma. A second-order accurate immersed boundary method for fully resolved simulations of particle-laden flows. *J. of Comput. Phys.*, 231:4469–4498, 2009.
[48] S. Tanguy and A. Berlemont. Application of a level set method for simulations of droplet collisions. *Int. J. Multiph. Flow*, 31:1015–1035, 2005.
[49] X.-D. Liu, R.P. Fedkiw, and M. Kang. A boundary condition capturing method for poisson's equation on irregular domains. *J. of Comput. Phys.*, 160:151–178, 2000.
[50] F. Denner and B.G.M. van Wachem. Numerical time-step restrictions as a result of capillary waves. *J. of Comput. Phys.*, 285:24–40, 2015.
[51] S. Popinet. An accurate adaptive solver for surface-tension-driven interfacial flows. *J. of Comput. Phys.*, 228:5838–5866, 2009.
[52] A. Prosperetti. Motion of two superposed viscous fluids. *Phys. Fluids*, 24:1217, 1981.
[53] J. R. Grace. Shapes and velocities of bubbles rising in infinite liquids. *Transactions of the Institution of Chemical Engineering*, 51:116–120, 1973.
[54] M. van Sint Annaland, N.G. Deen, and J.A.M. Kuipers. Numerical simulation of gas bubbles behaviour using a three-dimensional volume of fluid method. *Chemical Engineering Science*, 60:2999–3011, 2005.
[55] S. Asakura and F. Oosawa. Interaction between particles suspended in solutions of macromolecules. *Journal of Polymer Science*, XXXIII:183–192, 1958.
[56] P. Melby, A. Prevost, D.A. Egolf, and J.S. Urbach. Depletion force in a bidisperse granular layer. *Phys. Rev. E.*, 76, 051307:1–5, 2007.
[57] J.-C. Loiseau, O. Tammisola, and L. Brandt. Effect of viscosity ratio on the self-sustained instabilities in planar immiscible jets. *ArXive*, 1701.02972, 2017.
[58] M.S. Dodd and A. Ferrante. On the interaction of taylor length scale size droplets and isotropic turbulence. *J. of Fluid Mech.*, 806:356–412, 2016.